



SOLar-STellar Irradiance Comparison Experiment II (SOLSTICE II): End-of-Mission Validation of the SOLSTICE Technique

Martin Snow^{1,2,3} · William E. McClintock¹ · Thomas N. Woods¹ ·
Joshua P. Elliott¹

Received: 27 January 2022 / Accepted: 30 March 2022 / Published online: 12 May 2022
© The Author(s) 2022

Abstract

The *SOLar-STellar Irradiance Comparison Experiment* (SOLSTICE: McClintock, Rottman, and Woods, *Solar Phys.* **230**, 225, 2005) onboard the *Solar Radiation and Climate Experiment* (SORCE: Rottman, *Solar Phys.* **230**, 7, 2005) observed ultraviolet solar spectral irradiance (SSI) from 2003–2020. This article gives an overview of the end-of-mission algorithms and calibration of SOLSTICE. Many of the algorithms were updated after the early mission, either due to an improved understanding of the instrument and the space environment, or due to operational constraints as the spacecraft systems aged. We validate the final official data version (V18) with comparisons to other observations and models. The SOLSTICE observations of the solar-cycle variability in the ultraviolet are compared to model estimates.

Keywords Chromosphere · Instrumentation and data management · Integrated Sun observations · Solar irradiance

This article belongs to the Topical Collection:
The Solar Radiation and Climate Experiment (SORCE) Mission: Final Calibrations and Data Products
Guest Editor: Thomas N. Woods

✉ M. Snow
msnow@sansa.org.za
W.E. McClintock
mcclintock@lasp.colorado.edu
T.N. Woods
tom.woods@lasp.colorado.edu
J.P. Elliott
joshua.elliott@lasp.colorado.edu

- ¹ Laboratory for Atmospheric and Space Physics, University of Colorado Boulder, 1234 Innovation Dr., Boulder CO 80303, USA
- ² South African National Space Agency, Hospital Street, Hermanus 7200, South Africa
- ³ Department of Physics and Astronomy, University of the Western Cape, Robert Sobukwe Road, Bellville 7535, South Africa

1. Introduction

The Sun's radiative output is the dominant direct energy input to the Earth's climate system (Kren, Pilewskie, and Coddington, 2017). About half of the total solar irradiance (TSI) is transmitted through the Earth's atmosphere and either deposits its energy at the Earth's surface or scatters back into space. However, ultraviolet (UV) wavelengths are mostly absorbed by the atmosphere before reaching the ground. Therefore, an accurate measurement of UV solar spectral irradiance (SSI) can only be made from space. The far ultraviolet (FUV: 115–200 nm) is absorbed in the thermosphere and mesosphere, while the middle ultraviolet (MUV: 200–300 nm) deposits its energy in the stratosphere. SSI is therefore an essential contribution to the understanding of the Earth's climate system (Stephens et al., 2012). MUV SSI in particular drives the creation and destruction of ozone (Heath and Schlesinger, 1986; Haigh, 1994).

Over the solar cycle, the FUV varies by more than 10%, with some wavelengths such as Lyman α varying by 60%. The solar-cycle variation of the MUV is generally only a few percent, but the Mg II lines near 280 nm change by more than 10% (Rottman et al., 2001; Snow and McClintock, 2005; Woods and DeLand, 2021; Woods et al., 2022).

1.1. SOLSTICE

Understanding the variability of that radiative-energy input requires measurements on as many time scales as possible, from transient events that last only a few hours to decades-long changes in the baseline irradiance. These measurements are the primary objective of the *SOLar-STellar Irradiance Comparison Experiment* (SOLSTICE: McClintock, Rottman, and Woods, 2005) onboard the *Solar Radiation and Climate Experiment* (SORCE: Rottman 2005; Woods et al. 2021). SORCE was launched in 2003 and made irradiance measurements for seventeen years. It was finally decommissioned in January 2020.

SOLSTICE is a grating spectrometer. Its design was described in detail by McClintock, Rottman, and Woods (2005). On the SORCE platform, there were two identical spectrometers: SOLSTICE A and SOLSTICE B. Each spectrometer had two channels: FUV and MUV. The two channels shared all optical elements except for the exit slits and detectors. The MUV channel also had two neutral-density filters that could be inserted or removed from the light path. The light was directed onto one of the two exit slits using a camera mirror on a bi-stable mechanism (see McClintock, Rottman, and Woods (2005) Figure 4).

Before launch, SOLSTICE was absolutely calibrated at the National Institute of Standards and Technology's Synchrotron Ultraviolet Radiation Facility III (Arp et al., 2000). McClintock, Snow, and Woods (2005) describes the responsivity calibration and its uncertainty for both solar and stellar modes. The ground calibration allowed SOLSTICE to make absolutely calibrated measurements of the program stars (Snow et al., 2013a).

The SOLSTICE technique for monitoring the loss of responsivity over time (Snow et al., 2005a) uses a small entrance aperture and an exit slit to observe the Sun during the daylight period of each orbit. During eclipse, the 0.1 mm square entrance aperture is replaced by a 16 mm diameter circular aperture, and the exit slit is replaced by a wide slit (0.75 mm FUV; 1.5 mm MUV). The instrument is then pointed at one of the program stars (McClintock, Rottman, and Woods, 2005) to measure the stellar irradiance. An ensemble of stable, bright, early-type stars was chosen as the irradiance reference for SOLSTICE. These stars are expected to be stable individually at the 1% level on timescales of centuries (Mihalas and Binney, 1981). The average irradiance of the ensemble will be stable at an even better level. Any stars that become unstable relative to the ensemble are easily identified using the fitting technique described in Section 3.1.1.

The exposure pattern on the optics is not exactly the same for solar and stellar modes, so an additional relative measurement of the responsivity as a function of position is collected on a regular basis. The summary of these measurements is described in more detail in Section 3. The uncertainties in modeling the long-term behavior of these calibration observations, i.e. the instrument degradation, is the subject of Section 3.2.

Before launch, both SOLSTICE A and SOLSTICE B were carefully calibrated on the ground (McClintock, Snow, and Woods, 2005), and the planned method for maintaining this calibration in flight was described by Snow et al. (2005a). The measurement equation and preflight estimates of the parameters of this equation are fully described in these references, so they will not all be repeated here for the sake of brevity. During the course of the long mission, many of the algorithms for calibration needed to be updated or redesigned. This article describes the algorithm changes that had the most significant impact on irradiance. The data available in the archive are Version 18, which was finalized in late 2020. A final Algorithms Theoretical Basis Document (ATBD) is available online through the University of Colorado's CUScholar archive: scholar.colorado.edu/concern/reports/rx913r207 (Snow et al., 2021).

The flexibility of an accurately calibrated irradiance instrument with a stellar mode of operation has allowed SOLSTICE to do more than just monitor the UV SSI. The stellar observations have been used to cross-calibrate other instruments (Snow et al., 2013a; Pauluhn et al., 2015; Gröller et al., 2018; Chaffin et al., 2018). Lunar-reflectance observations (Snow et al., 2013b) have been used in cross-calibration and are now being incorporated into a revised photometric model (Young et al., 2021). Comet P/Holmes observations presented an opportunity to cross-calibrate SOHO/SWAN (Pryor et al., 2013).

1.2. SORCE

The operation of the SORCE spacecraft is described in detail by Woods et al. (2021), but a few elements that are particularly relevant to the SOLSTICE data record are summarized here. Spacecraft-battery performance is crucial to the success of every mission, and the degradation of SORCE's batteries over its operational lifetime forced many changes to SOLSTICE's observations and its data-processing algorithms.

The loss of battery capacity after the first few years of operation required that instruments be switched off during the eclipse portion of the orbit. SOLSTICE A began power cycling during eclipse in 2008, followed by SOLSTICE B in 2010. The loss of the eclipse observations meant the end of stellar-irradiance measurements until very late in the mission (Section 3.2.1).

Additionally, there were two time periods when the loss of battery capacity caused the spacecraft to enter safe mode. The first was a six-week period at the end of 2011. The more important event started in mid-2013 and lasted until early 2014. During this spacecraft emergency, the flight software was reconfigured and the spacecraft began the Day Only Operation (DO-Op) mode. All instrument commanding was changed. The changes to each mode of data collection are described in the appropriate subsection.

2. In-Flight Operation

This section describes the routine and non-routine operation of the SOLSTICE instrument during the seventeen-year mission. The primary data product was a daily average spectrum of the disk-integrated irradiance corrected to 1 AU. This spectrum was published with the

full spectral resolution of the instrument (0.1 nm, sampled every 0.025 nm) as well as a version binned to 1-nm intervals. This daily average with all corrections is referred to as Level 3 (L3) and is available on the LASP Interactive Solar Irradiance Datacenter (LISIRD: lasp.colorado.edu/lisird/) as well as from the NASA archive (acdisc.gesdisc.eosdis.nasa.gov/data/SORCE_Level3/SOR3SOLFUV.018/). These data products are described more fully in Section 2.2.

2.1. Overview of Observations

Routine operations of the two SOLSTICE instruments began after a two-month commissioning phase. The full dataset begins in April 2003. During the primary mission, the two spectrometers (SOLSTICE A and B) would each measure SSI on nearly every orbit, with SOLSTICE A observing the MUV channel and SOLSTICE B scanning the FUV. In this way, the full spectral range was captured on each orbit. Once per week, the two spectrometers made cross-calibration measurements of both channels on a single orbit. Later in the mission, this cross-calibration was performed every day.

The spectral resolution of each channel was nearly the same (0.1 and 0.09 nm, McClintock, Snow, and Woods, 2005 (Table 1)). A normal spectral scan sampled the spectrum at standard grating-drive angular positions every 0.03 nm. Due to the difference in responsivity, the integration time in the FUV was 1.0 second and the MUV integration time was 0.5 second. Figure 5 of McClintock, Snow, and Woods (2005) shows the absolute responsivity of the different configurations for both spectrometers.

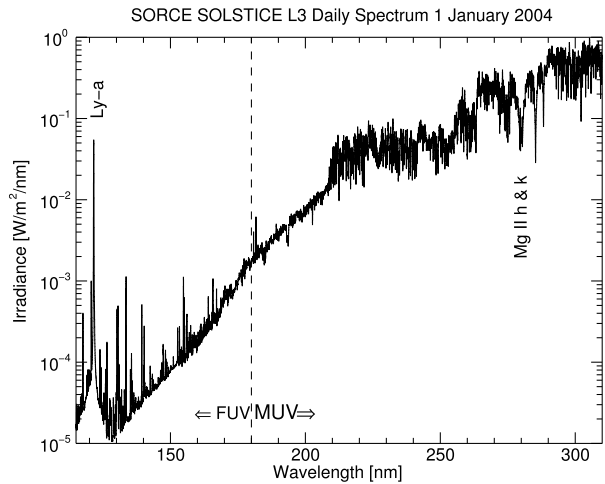
A typical day included Normal spectral scans (Section 2.1.1) on the majority of orbits. One orbit each day was devoted to wavelength calibration, and two orbits were devoted to thermal calibration. The wavelength calibration involved a repeating spectral scan over a small range (Section 2.1.2), while the thermal calibration was performed at a fixed wavelength for the entire orbit to measure the change in detector gain as a function of temperature.

2.1.1. Normal Spectral Scans

The most common mode for SOLSTICE to measure the solar spectrum is referred to as a Normal scan. The algorithm for determining the wavelength from the grating angle has been updated since McClintock, Rottman, and Woods (2005), and it is described in Section 3.3.1. The FUV Normal scan begins at about 113 nm and extends to 192 nm. The MUV Normal scans run from 155 to 317 nm. These scan ranges extend to the edges of the responsivity for each channel, and they allow for a large overlap between the two. The public data products go from 115–180 nm for the FUV and 180–310 nm for the MUV. The small regions at short and long wavelengths do not have sufficient signal-to-noise ratio to warrant publication. Figure 1 shows a typical daily spectrum.

After the spacecraft emergency in 2013 (Woods et al., 2021), instrument operations were dramatically altered for SOLSTICE. Instead of orbits consisting of several types of scans and calibration activities with SOLSTICE A dedicated to MUV observations and SOLSTICE B dedicated to the FUV, both A and B ran identical activity plans each orbit. This new activity consisted of a spectral scan with a reduced integration time (from 1000 down to 500 ms for FUV, and from 500 down to 200 ms for MUV) followed by a short interval of wavelength calibration scans (see Section 2.1.2 for descriptions of these wavelength calibrations). The observing strategy would ensure that in any orbit with 20+ minutes of *Tracking and Data Relay Satellite System* (TDRS) contact for data download, we would get a full spectrum plus the wavelength-calibration scans. Both instruments observed in the same FUV/MUV mode

Figure 1 Typical daily average spectrum from SORCE/SOLSTICE, covering 115–310 nm. The important H I Lyman α (121.6 nm) and Mg II h and k lines (280 nm) are indicated.



and then switched to the other mode on the following orbit. The data volume was greatly reduced compared to the prime mission, but all requirements for creating a valid Level 3 spectrum each day were met.

2.1.2. Wavelength Calibration Scans

The wavelength-calibration orbits consisted of repeated measurements of one spectral feature. In the FUV, the Lyman α line (121.6 nm) was repeatedly scanned with a repeat cadence of about one minute. These Lyman α scans are now available as a separate data product from the SORCE web page: lasp.colorado.edu/home/sorce/data/. Initial results of these calibration observations have been included in several publications on solar flares (Woods et al., 2004; Milligan and Chamberlin, 2016) as well as a study on exospheric hydrogen (Pierrat, Snow, and Machol, 2016). The SUMER Lyman α line profile was convolved with the SOLSTICE instrument profile to calibrate the high-resolution model of Kretzschmar, Snow, and Curdt (2018). A detailed description of the data product and additional scientific results is in preparation.

In the MUV, the chosen spectral region was the Mg II doublet near 280 nm (Snow et al., 2005b). In the first few years of operation, the MUV repeat cadence was about 2.5 minutes. An observation of a strong flare with the instrument in this high-cadence mode (Woods et al., 2004) showed that such Mg II observations have scientific merit. As described by Snow and McClintock (2005) and Snow et al. (2009), the variations in the Mg II cores warranted higher cadence observations than the 2.5-minute scan. The daily wavelength-calibration scan was modified to repeat the core measurement every 45 seconds. The wing reference irradiance was measured at the beginning and end of these orbits, but the majority of the time was spent scanning only the emission cores.

2.2. Data Products

The data-processing system takes advantage of the oversampling to create the primary data product from the SOLSTICE instrument. All of the spectral scans from each 24-hour period are aggregated and fitted with a high-order basis spline function. There are now two versions of the L3 data product, both derived from this spline fitting. The full-resolution spectrum

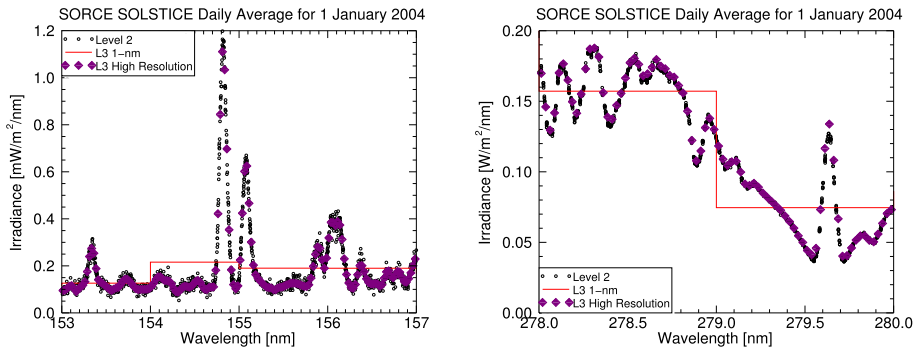


Figure 2 SOLSTICE data-product comparison. This small wavelength range shows the Level 2 data from the FUV channel (*left*) and the MUV channel (*right*). The *small open circles* are the fully corrected Level 2 irradiance data gathered during the 24-hour period on 1 January 2004. The *filled diamonds* show the irradiances from the new full-resolution data product. It was produced on a regular 0.025 nm wavelength grid. For comparison, the standard 1-nm-binned L3 data product is shown in *red*.

evaluates the spline function on a uniform wavelength grid with a spacing of 0.025 nm (Snow and Elliott, 2021; Snow et al., 2021). These higher-resolution data were used to create new SSI models (Chamberlin et al., 2020), and they have been used extensively in planetary-atmosphere analysis (Roth et al., 2021; Molyneux et al., 2020; Jessup et al., 2020, 2015; Cunningham et al., 2015).

The 1-nm-binned data product is derived from a numerical integration of the spline function over 1-nm intervals. Figure 2 shows the Level 2 data used in the spline fitting, the high-resolution L3 data product and the standard 1-nm data for a small region of the FUV (*left*) and MUV (*right*) spectrum. For wavelength regions with narrow features, the high-resolution L3 allows a much more detailed analysis of the spectrum. Both L3 data products are available on a daily basis for the entire SOLSTICE mission in both channels. The integration over 1-nm intervals is the same algorithm used for the previous SOLSTICE onboard the *Upper Atmosphere Research Satellite* (UARS: Rottman, Woods, and Sparn, 1993). Daily 1-nm irradiances from the two missions can therefore be directly compared.

The data are available on the SOLSTICE web page lasp.colorado.edu/home/sorce/data. The 1-nm data file is available as an IDL save file and as an ASCII text file. The irradiance uncertainty is the root-sum-squared (RSS) combination of the calibration uncertainty (McClintock, Snow, and Woods, 2005) and the repeatability (Taylor and Kyuatt, 2001). Since there are many samples in each 1-nm interval during a 24-hour period, the statistical uncertainty is small, and the total uncertainty is dominated by the calibration uncertainty. The calibration uncertainty includes both preflight absolute calibration and uncertainty in the degradation correction.

The full-resolution data product is available in NetCDF format. In order to keep the file size manageable, the data are split into yearly files, each about 50 MB. The full-resolution data include two uncertainty estimates; one is the combined uncertainty (calibration and measurement), and the other is the measurement uncertainty alone, i.e. repeatability. The uncertainty in degradation correction is time-dependent, and it is therefore much more complicated. Section 4 discusses irradiance uncertainty in more detail.

3. In-Flight Calibration

As described by McClintock, Snow, and Woods (2005), SOLSTICE was carefully calibrated before launch. The plan to maintain this calibration on orbit through observations of standard stars and relative measurements across the instrument's field-of-view (FOV) is fully described by Snow et al. (2005a). These two methods are briefly revisited in Section 3.1. As the mission progressed, operational constraints required modifications to these observation plans. The new algorithms and observations are described in Section 3.2.

3.1. Calibrations During the Primary Mission

3.1.1. Stellar Fixed Wavelength Observations

The primary means of maintaining SOLSTICE's calibration on-orbit was by observing of bright early-type stars (McClintock, Rottman, and Woods, 2005; Snow et al., 2005a). During the eclipse portion of every orbit, the instrument configuration was changed from solar to stellar. This involved swapping entrance and exit slits, removing the MUV neutral-density filters and taking longer integrations. Over time, the observing plan cycled among an ensemble of stars, taking measurements at fixed wavelength positions. Figures 5 and 6 of Snow et al. (2005a) show the wavelengths used in the stellar calibrations. Snow et al. (2005a) was published early in the SORCE mission, so the time series shown in Figures 11 and 12 of that article show a limited time range. Figures 3 and 4 shown here are typical stellar irradiance time series over the mission. These wavelengths were chosen from the middle of each channel's wavelength range and are typical for all wavelengths in the two observing modes.

The four panels of Figures 3 and 4 are as follows: The upper-left panel shows the uncorrected stellar irradiances at this wavelength. The spectral resolution of SOLSTICE in stellar mode is about 1 nm in the FUV and 2 nm in the MUV (McClintock, Snow, and Woods, 2005). The primary assumption of the SOLSTICE technique is that the stellar irradiance is constant, so that any measured changes observed in the stellar signals are due to instrument degradation (Snow et al., 2005a). The degradation rate is assumed to be the same for each star. A least-squares fit is done on the ensemble of stellar measurements using MPFIT (Markwardt, 2009) where each star's apparent magnitude is a free parameter [A_0] but there is one set of time constants [β and τ] that apply to all. The degradation function is assumed to be a simple exponential:

$$d(t) = A_0(1 - \beta + \beta e^{-t/\tau}). \quad (1)$$

t is the time since launch, and the degradation factor d is unity at $t = 0$ since each star's irradiance is normalized by A_0 . τ and β are fitting parameters describing the decay time constant and asymptote of the exponential function (Snow et al., 2005a).

The lower-left panel of Figure 3 shows the stellar data after normalization, the best-fit line (solid), and the 1- σ uncertainty ($k = 1$) envelope on this fit. The uncertainty in the fit can be interpreted as one component of the uncertainty in the long-term degradation correction. The uncertainty in the degradation fit at the measured wavelength grows at about 0.2% per year. It is not a strong function of wavelength. The uncertainties are discussed in more detail in Section 4.

The upper-right panel is the histogram of the residuals after applying the degradation correction to the stellar irradiances. The smooth curve is a Gaussian fit to the histogram, and the reduced χ_v^2 is determined from the deviation from this model. At each wavelength, χ_v^2

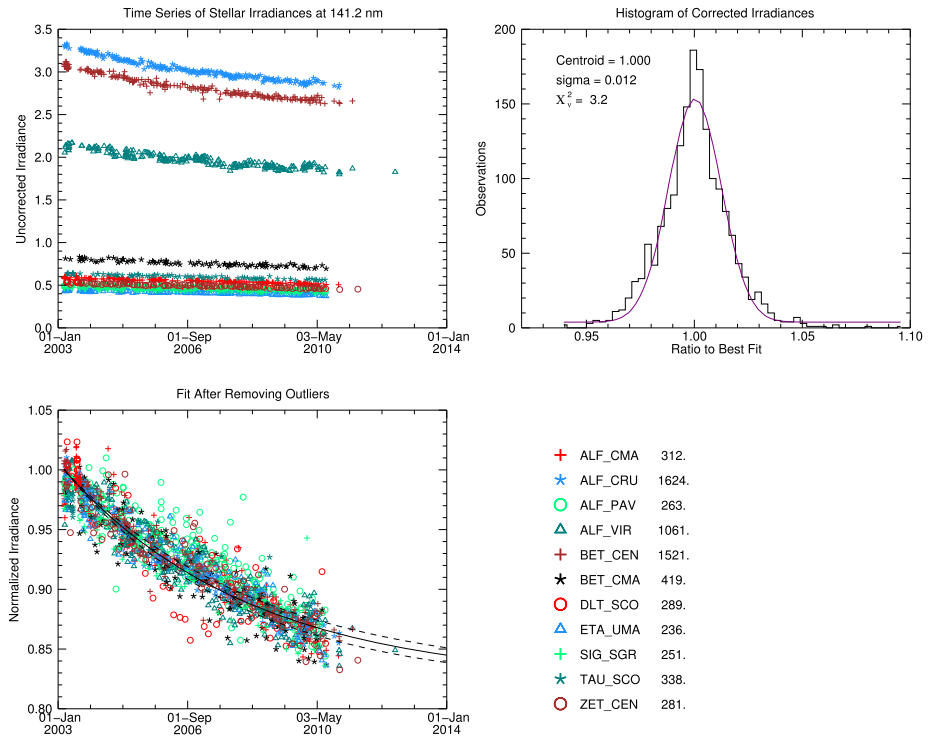


Figure 3 Stellar observations for the FUV channel at 141.2 nm. The *upper-left panel* shows the uncorrected stellar irradiances in 10^4 photons $\text{cm}^{-2} \text{s}^{-1} \text{nm}^{-1}$ for all stars used for the fit at this wavelength. The *lower left panel* shows the stellar measurements after normalization and curve fitting. The *solid line* shows the best fit exponential, and the *two dashed lines* show the $k = 1$ uncertainty envelope for the fit. The *upper-right panel* shows the histogram of residuals for the best fit. The *table in the lower right* is the legend for the two time series, showing the symbol, the name of each star, and the average count rate at this wavelength.

is of order unity, indicating that there is no need to reject the assumption that the residuals are normally distributed. We interpret this result as confirmation that our exponential model for the degradation (Equation 1) is a good representation of the trends in the stellar data.

Below the histogram, the names of the stars used at that wavelength are identified by plot symbol, and the average count rate is given. Stars with lower count rates were observed for many one-second integrations, so that each stellar observation had about a 1% statistical uncertainty (Snow et al., 2005a).

Two differences between the FUV and MUV stellar observations are important to notice: First, many fewer stars are used in the MUV fit. Not as many program stars are bright in the MUV. Second, the rate of degradation between the two channels is significantly different. The MUV channel degraded at a much slower rate than the FUV channel. It should be noted that the stellar observations stopped in 2010 due to spacecraft-battery degradation (Woods et al., 2021). The exponential functions from the first six years had leveled out for all wavelengths, so these functions were extrapolated to the end of the mission.

In addition to fixed-wavelength observations at a limited number of wavelengths, SOLSTICE also made continuous stellar spectral scans (Snow et al., 2013a). These scans were useful for astronomical instrument cross calibrations as mentioned in Section 1.1, but they were also critical in validating the late-mission degradation that is described in Section 3.2.1.

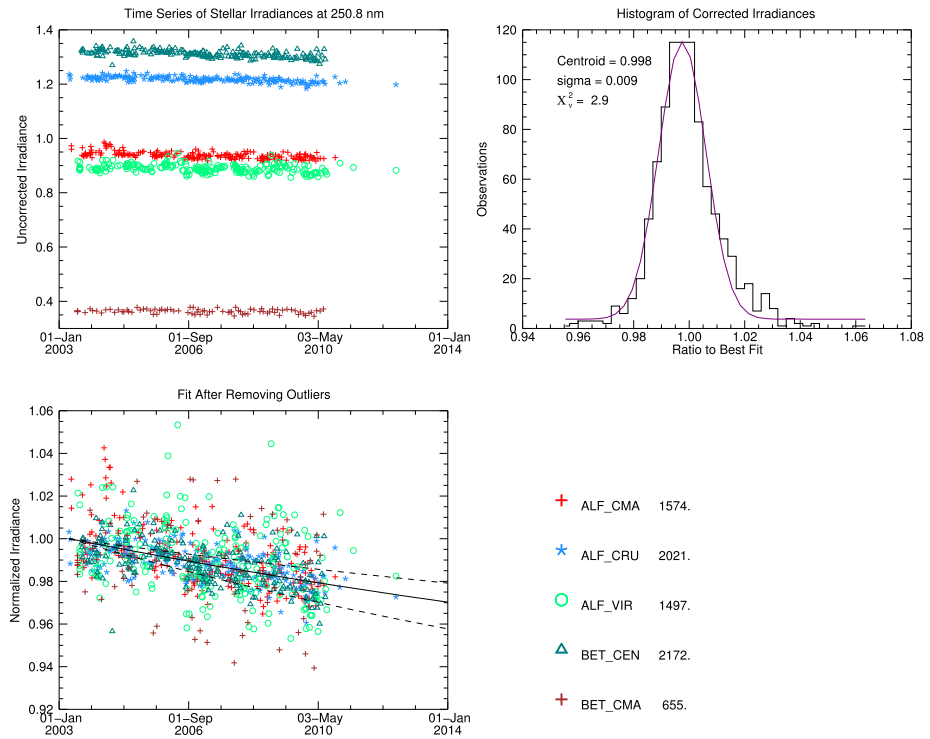


Figure 4 Stellar observations for the MUV channel at 250.8 nm. The *upper-left panel* shows the uncorrected stellar irradiances in $10^4 \text{ photons cm}^{-2} \text{ s}^{-1} \text{ nm}^{-1}$ for all stars used for the fit at this wavelength. The *lower-left panel* shows the stellar measurements after normalization and curve fitting. The *solid line* shows the best-fit exponential, and the *two dashed lines* show the $k = 1$ uncertainty envelope for the fit. The *upper-right panel* shows the histogram of residuals to the best fit. The *table in the lower right* is the legend for the two time series, showing the symbol, the name of each star, and the average count rate at this wavelength.

3.1.2. Field-of-View Observations

In addition to observations of bright stars, the SOLSTICE technique requires a relative measurement of the responsivity over the FOV (Snow et al., 2005a). The stellar-observing configuration uses a collimated beam of starlight that exposes the optics differently than the diverging beam of sunlight. Harsh sunlight degrades a relatively small spot on the primary mirror, and there is a pristine, larger, circular region that sees only starlight. The ratio between these two zones is a multiplicative factor in the degradation term of the solar-irradiance measurement equation.

During the primary mission, the measurement of the degradation of the larger circular region was made by slewing the spacecraft and letting the Sun cross the stellar FOV (Snow et al., 2005a). Figure 5 shows the signal as a function of slew angle in the cross-dispersion direction for a typical observation. The shaded region shows the portion of the FOV that is normally exposed to sunlight. As the slew angle increases in either direction, the solar image is vignetted by the internal baffles and the signal drops to zero. The FOV measurement is the ratio of the signal at the shoulders of edge of the plateau to the signal at the center (Snow et al., 2005a).

Figure 5 Example field-of-view measurement. The instrument observed at a fixed grating position while the spacecraft slewed across the Sun. The *shaded region* shows the portion of the FOV that is normally exposed to sunlight.

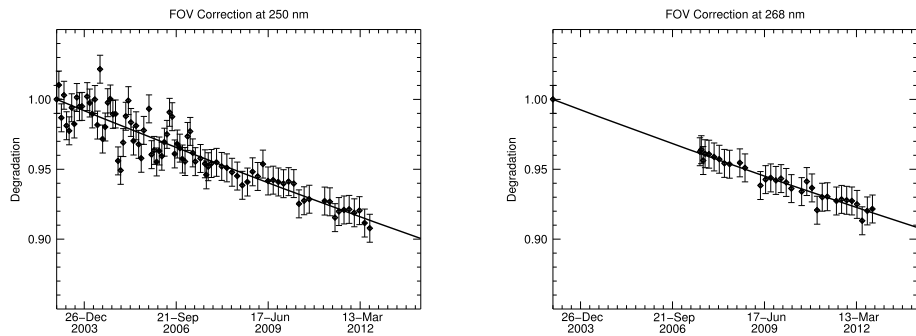
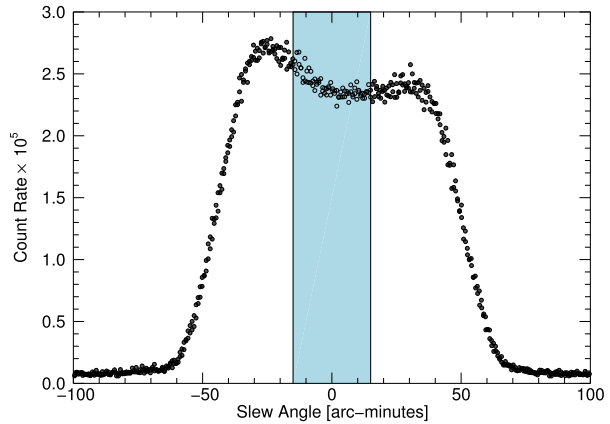


Figure 6 Field-of-view measurements of the primary mission derived from weekly cruciform scans. Measurements later in the mission (from 2007 onwards) had smaller random errors due to better wavelength information. The wavelength shown in the *left panel* was observed starting at the beginning of the mission. The wavelength shown on the *right* was added later and extrapolated up to launch. The normalization of the data is discussed in the text in Sections 3.1.2 and 3.2.2.

These observations were made at four wavelengths in each channel at the beginning of the SORCE mission. Once it became clear that the FOV correction was a significant contribution to the total degradation correction for the MUV, an additional four wavelengths were added to the planning software. One orbit per week was devoted to solar slews in the spacecraft yaw and pitch directions. A different wavelength was chosen each week so that the observation cycle would repeat every eight weeks. Figure 6 shows the time series of the FOV correction for two wavelengths. The left panel shows a wavelength observed since the start of the mission. The right panel shows a wavelength that was added later.

As described by Snow et al. (2005a), the center of the FOV was somewhat degraded during ground calibration, so all results are normalized to the first on-orbit measurements. For wavelengths that were added partway through the mission, extrapolating back to the beginning introduces some additional uncertainty in the early degradation correction. Version 18 mitigated this uncertainty with a new algorithm (Section 3.2.2).

One additional algorithm change that is relevant to this section was the change from commanding a fixed grating position during the spacecraft slew to commanding a spectral scan with a high repetition cadence. The wavelength range was kept small so that the same

wavelengths would be resampled many times throughout the maneuver. One of the sources of uncertainty in these FOV observations was that the exact wavelength sampled could be different from week to week (Snow et al., 2005a). Another source of uncertainty was that the wavelength scale shifted as a function of angle. Depending on the local spectral shape, the irradiance could go up or down due to small changes in the observed wavelength. Changing to a small spectral scan allowed us to correct for this wavelength shift. The reduction in uncertainty for each weekly measurement can be seen in the left panel of Figure 6. The data for the observations before 2007 have a much larger scatter than the later observations.

An important consideration is that the FOV correction was not as significant for the FUV channel. The FUV stellar observations showed a degradation of up to 15% due to detector fatigue. Changes to the FOV correction were of the order of 1–2% above 170 nm, and even less at shorter wavelengths. The analysis of the 170–180 nm range of the FUV channel is still ongoing and will be part of a Solar Irradiance Science Team project.

3.2. Changes to Calibration Observations and Degradation Model During Day Only Operation (DO-Op) Mode

Calibration measurements in the Day Only Operation (DO-Op) period needed to be changed to meet the new operational constraints. Battery degradation had forced the SOLSTICE instruments to be powered off during eclipse starting in 2008, and spacecraft commanding had to be greatly simplified after the spacecraft emergency in 2013 (Woods et al., 2021). The measurements described by Snow et al. (2005a) for stellar and FOV had to be reconfigured. Sections 3.2.1 and 3.2.2 describe the new observing sequences.

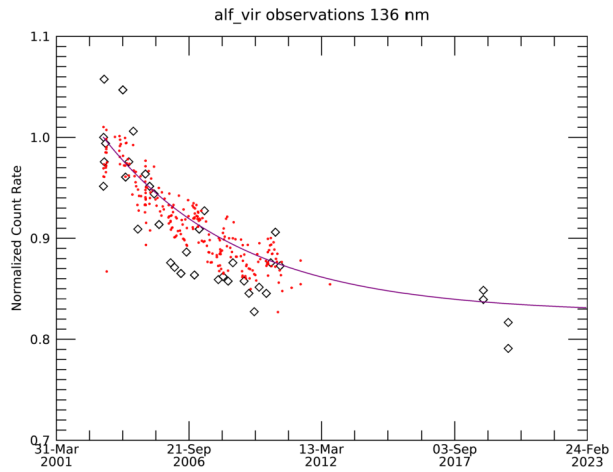
3.2.1. DO-Op Stellar Observations

After an entrance-aperture anomaly on SOLSTICE A at the beginning of 2006 (Snow et al., 2021), all stellar measurements fell to SOLSTICE B only. SOLSTICE A was able to continue to make dark measurements during the eclipse between 2006 and 2008, but not stellar-irradiance observations. The eclipse portion of every orbit was devoted to stellar and dark-sky observations. However, the spacecraft's batteries began to degrade. To keep the mission going, the science instruments had to be powered off during eclipses starting in 2009 (Woods et al., 2021). Without eclipse operations, we could not make stellar-irradiance observations. The degradation correction derived from the first six years of stellar measurements was extrapolated to the end of the mission.

In order to validate that the extrapolation was reasonable, late in the mission we were able to execute a few stellar observations during the daylight part of the spacecraft orbit. The constraints on selecting a stellar target were that the angular distance from the Sun had to be at least 20° but not more than 30°. The first criterion was to keep the sunlight out of the FOV entirely, and the second criterion was to keep the solar panels illuminated. The low battery capacity needed to be fully restored every orbit, so the loss of sunlight on the solar panels needed to be minimized. Therefore, there was a ten-degree wide annulus around the Sun that would allow DO-Op stellar observations.

With these observing constraints, there were very few opportunities for stellar observations. In fact, we were only able to make stellar measurements in DO-Op mode twice. So we needed to maximize the scientific benefit. Since the MUV degradation curves were very shallow compared to the FUV curve, we observed only the FUV. Rather than cycle through the 18 fixed-wavelength points of the FUV stellar observing plan (Snow et al., 2005a), we instead commanded a continuous stellar spectral scan. Stellar spectral scans had also been

Figure 7 Time series of the uncorrected stellar fluxes from α Virgo at 136 nm. *Red dots* indicate the fixed-wavelength observations from the primary mission, and the curve is the exponential fit derived from them. The *diamonds* indicate observations from spectral-scan experiments from the primary mission and the DO-Op periods. The DO-Op scans are consistent with trends observed during the primary mission.



performed during the primary mission (Snow et al., 2013a) so that the late-mission observations could be directly compared. α Virgo was chosen as the primary stellar target for DO-Op observations, because it is bright and its location in the sky was compatible with the angular requirements.

Figure 7 shows the apparent brightness of α Virgo near 136 nm as a function of time. The red dots are the fixed-wavelength observations from the primary mission. The curve is the exponential fit through the fixed-wavelength observations. The black-diamond symbols show the observations from stellar scans, both during the main mission and during DO-Op mode. The statistical uncertainty in each of the stellar scans is lower than in the fixed-wavelength observations due to fewer integrations at each wavelength dwell (Snow et al., 2005a).

The DO-Op stellar measurements are consistent with the extrapolated degradation curve. There are not enough measurements to warrant rejecting the fit from the primary-mission data. The exponential curves at each wavelength in the later part of the mission have small slopes, indicating that the rate of degradation had slowed after the first few years of operation. The stellar component of the Version 18 degradation function is the same function that had been used in the data versions since the end of the primary mission in 2008.

An additional means of validating the SOLSTICE FUV degradation was a rocket under-flight of *Compact SOLSTICE* (CSOL) in 2018 (Thiemann et al., 2022). This small instrument was designed to provide an end-of-mission calibration for SOLSTICE, since stellar observations were a challenge. The rocket flight did provide a FUV spectrum, but an operational anomaly caused the MUV spectrum to be overexposed and saturated the detector. CSOL will be launched again on the *INSPIRESat-3* mission in 2022 (Thiemann et al., 2022).

Lyman α irradiance measurements from the GOES-R series *Extreme ultraviolet and X-ray Sensor* (EXIS) instruments (GOES-16 and GOES-17) agreed with SOLSTICE (Machol et al., 2020) to within a few percent at first light. The degradation corrections after launch used SOLSTICE trending, so no comparison of the long-term trends between instruments is useful.

3.2.2. DO-Op Field-of-View Correction

The other major algorithm change mandated by the DO-Op mode was to the FOV observations. Weekly cruciform slews could no longer be commanded, so an alternative means of

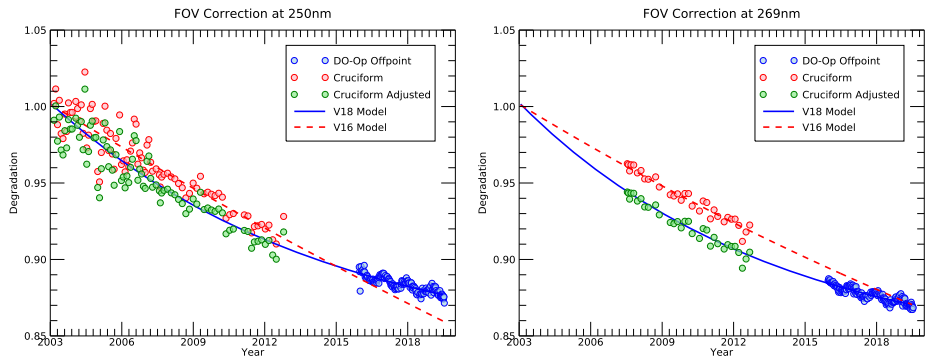


Figure 8 DO-Op offpoint and standard FOV measurements at 250 nm (*left*) and 268 nm (*right*). *Red* symbols and *red* curve are the FOV measurements and curve fit shown in Figure 6 for these wavelengths. The *blue* symbols show the measurements from DO-Op offpoint scans. The *blue* curve is the new FOV degradation curve after adjustment of the normalization of the primary-mission data. The adjusted data are shown in *green*.

measuring the FOV degradation was required. Our solution was to make a single offpoint from the solar boresight to 26 arcminutes away. The drawback of not sampling the entire FOV was more than made up for by the advantage of a long dwell time at the offpoint. Instead of asynchronously making a small wavelength scan during the slew, the instrument could now make a spectral scan of the entire MUV wavelength range. We gained FOV information at every wavelength, not just at four or eight selected wavelengths.

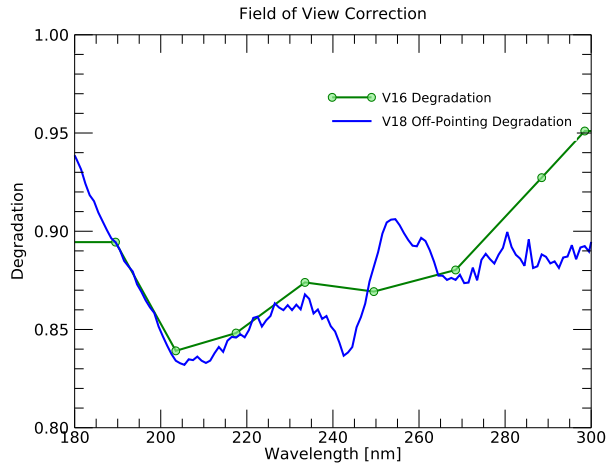
As discussed by Snow et al. (2005a) and Section 3.1.2, the preflight shape of the FOV was not well measured, and the relative measurements taken in flight were all normalized to make the correction unity at the beginning of the mission. Figure 8 shows the time series of FOV measurements for one wavelength. The red circles and the red curve are the data shown in the left panel of Figure 6. The blue points are the data measured with the DO-Op offpoint maneuver. The slope of the DO-Op data was not consistent with the primary-mission observations. However, if the normalization factor for all of the primary-mission data was allowed to be a (single) free parameter in a multivariate fit for the two datasets, a single exponential fit could be determined. The green circles show the main mission data with the new normalization factor applied, and the blue curve is the final FOV degradation function for this wavelength.

As discussed in Section 5.4, one of the areas of disagreement between SOLSTICE and other irradiance measurements and models was the steep decrease in the MUV during the decline of Solar Cycle 23. The renormalization of the primary-mission FOV measurements to align with the DO-Op FOV measurements steepens the early-mission degradation curve, thus reducing the decline of SSI during that part of the mission.

Figure 9 shows the tremendous gain in information about the FOV correction as a function of wavelength due to replacing the eight individual wavelengths with a spectral scan. Previous measurements at 230 nm, 250 nm, and 270 nm completely missed the features in between. Without the DO-Op version of the FOV measurement, we would have never solved the mystery of the anomalous solar-cycle variations in the MUV channel.

The other region of significant disagreement between the primary-mission cruciform scans and the DO-Op offpoint is for wavelengths longer than 280 nm. The DO-Op data show much more degradation than the extrapolation of the cruciform time series. There is a gap of several years between the end of the cruciform observations and the beginning of

Figure 9 Comparison of the FOV measurements from the eight wavelengths and the full spectral scan. The inferred degradation function was linearly interpolated between the eight wavelengths, leading to a loss of information between 230 and 260 nm. The eight wavelengths were used up to Version 16. Starting with Version 17, the full spectrum was used.



the DO-Op offpoints, as shown in Figure 8. The SSI at those wavelengths in earlier versions of the SOLSTICE data showed a steady decline with time that was not consistent with the energy input to the atmosphere (Ermolli et al., 2013). Therefore, we made the decision to adopt the DO-Op measurement of the FOV degradation instead of the extrapolated cruciform trend.

The additional information as a function of wavelength from the DO-Op FOV measurements was also used to better inform the shape of the degradation surface during the primary mission. Rather than just linearly interpolating between observed wavelengths, as was done prior to Version 17, the shape shown in Figure 9 was propagated back to the beginning of the mission in the Version 18 data product.

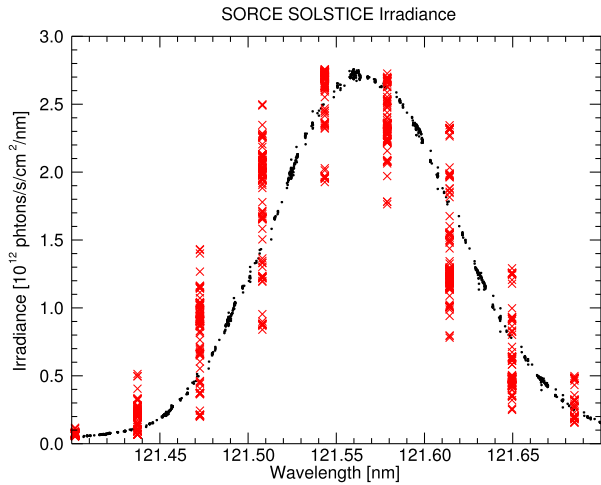
3.3. Additional Algorithm Changes During the SOLSTICE Mission

Spacecraft operations over the long, seventeen-year mission forced many changes to the algorithms described by McClintock, Rottman, and Woods (2005), McClintock, Snow, and Woods (2005), and the preflight Algorithm Theoretical Basis Document [disc.gsfc.nasa.gov/information/documents?title=SOLSTICE Mission Preservation Documents](https://disc.gsfc.nasa.gov/information/documents?title=SOLSTICE%20Mission%20Preservation%20Documents). This section describes the changed algorithms that had the largest impact on the final data products. There are also many other smaller algorithm improvements described in the SOLSTICE updated ATBD (Snow et al., 2021) and version release notes (Snow and Elliott, 2021). The ATBD includes short-term corrections for the SOLSTICE A entrance-aperture anomaly in 2006, SOLSTICE B aperture events in 2006, and transition to the DO-Op mode in 2014, as well as updates to the thermal model, detector dead time, filter transmission, and DO-Op exposure time. It also includes a description of the architecture of the data-processing system.

3.3.1. Wavelength Scale

The step size of a normal scan is as described by McClintock, Snow, and Woods (2005), i.e. 33% of the solar-mode spectral bandpass. Equation 27 of that article (the grating equation) shows the conversion of grating position to wavelength for the solar mode; however, this relationship does not take into account Doppler shifts due to the orbital motion of the spacecraft. These Doppler shifts can be as large as one-third of a grating step. The final algorithm

Figure 10 A section of the spectrum with repeated measurements over the course of an orbit with and without correction for spacecraft Doppler motion. *Red Xs* show the estimated wavelength from the grating equation and the range of irradiances that would have been reported at those uncorrected wavelengths. The *black dots* are the same irradiance values, but with the corrected wavelength.



uses the spacecraft velocity vector throughout the orbit to shift each sample to the correct wavelength. Figure 10 shows the result of the Doppler correction for a series of many observations over the same wavelength range throughout an orbit. Taking the Doppler shifts into account, the wavelength sampling over the course of a day is much better than the 33% of the spectral bandpass for a single scan.

3.3.2. South Atlantic Anomaly

The photomultiplier tubes used as detectors in the SOLSTICE instrument are sensitive to high-energy particles such as those in the Earth's radiation belts. The South Atlantic Anomaly (SAA: Pavón-Carrasco and De Santis, 2016) is a region where the radiation belts dip down to lower altitudes, intersecting the orbit of SOLSTICE. The original method for removing contamination from the SAA was to use a static geographic map to identify observations that might be corrupted and remove them from the data-processing stream. This was the algorithm for correcting UARS/SOLSTICE data, and in fact the same static map was planned for use by SOLSTICE/SOLSTICE. Continued observations of the SAA determined that it was not a static geomagnetic feature and that a more dynamic means of detecting it would be appropriate. The design of SOLSTICE/SOLSTICE uses one observing (active) channel at a time for irradiance measurements. The other (inactive) channel is read out at the same time. Since the optical chain sends light to only one channel at a time, the inactive channel's counts are the result of the dark count rate and particle hits. Figure 11 shows a map of the historical SAA region and measurements of the inactive channel during the eclipse portion of the SOLSTICE orbit for two weeks in 2003. The data are plotted in geomagnetic coordinates.

The elevated background level is clearly visible with background counts rising from order unity to many thousands. The red diamond shows the estimated center of the SAA based on these measurements. The evolution of the SAA seen in these SOLSTICE measurements shows that the center moving westward at about $0.33^\circ \text{ year}^{-1}$ and northward about $0.16^\circ \text{ year}^{-1}$.

The revised algorithm for SOLSTICE/SOLSTICE uses the background level of the inactive channel to flag corrupted integrations. The primary advantage of using the inactive channel is that it is a real-time measurement of the particle background and does not depend on the SAA remaining within a static geographic region. The full description of the SAA analysis

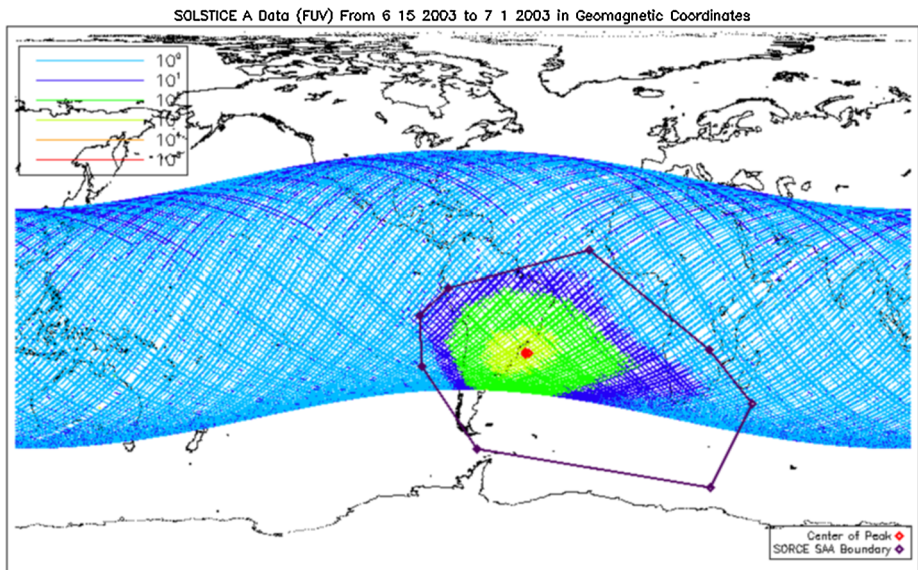


Figure 11 Background count rates from the inactive channel during eclipse observations over a two-week period in 2003. The original (static) boundary of the SAA is indicated by the *black line*, and the center of the SAA is shown by the *red diamond*. The data are plotted in geomagnetic coordinates.

will be published in a future article. Initial results were presented by O'Connor and Snow (2011).

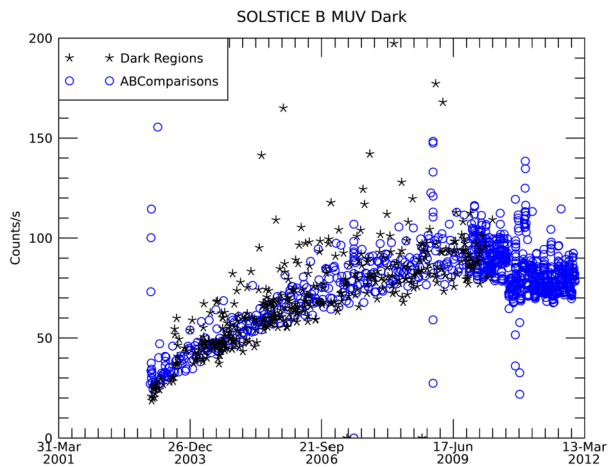
3.3.3. Dark Counts

The algorithm for measuring the detector dark counts has also been changed since the article by Snow et al. (2005a). Originally, dark counts were measured during special stellar observations of star-free regions of the sky. These measurements were then averaged and fit with a spline curve in time (cf. Figure 4 of Snow et al. (2005a)).

The FUV detectors showed a low dark rate (a few per second) consistent with preflight measurements. The FUV dark count rate remained unchanged throughout the mission. As described by Snow et al. (2005a), the MUV dark rate was much higher on orbit than was seen in preflight testing. The detector dark count rate in the MUV channels of both instruments was found to be slowly increasing over the first several years of the mission, reaching a plateau in 2009. The MUV dark rate remained relatively constant for the remaining decade of the mission, so that the dark rate was not a simple function of solar activity. The physical cause of these changes in the dark count rate is still unknown.

Degradation of the spacecraft's batteries led to the cessation of all routine eclipse observations in 2009, so an alternative method of monitoring the dark count rate was needed. The new algorithm uses the inactive-channel measurements described in Section 3.3.2 rather than eclipse observations. Up to 2010, a cross-calibration observation sequence known as "AB-Comparison" consisted of simultaneous scans in both FUV and MUV mode for both SOLSTICE A and SOLSTICE B. The purpose of these simultaneous observations of the Sun is to allow us to transfer the calibration from one instrument to the other. AB-Comparison experiments were performed weekly from launch until 2010, when the cadence was increased to daily. So an inactive-channel measurement of the dark rate was made for each

Figure 12 Detector dark count rate for the SOLSTICE B instrument in MUV mode. *Black stars* are observations of star-free regions of the sky during the eclipse. The *blue circles* are from the inactive channel during the daytime AB-Comparison experiments.



instrument in solar mode at least once per week for the entire mission. Figure 12 shows the eclipse dark-region measurements in black and the inactive-channel dark rate measurements in blue for the first half of the mission. Both types of dark-rate measurements are consistent during the time period when eclipse measurements were possible.

3.3.4. 1-AU Correction

The standard irradiance data products from SOLARIS/SOLSTICE are all corrected to the average Sun–Earth distance, i.e. to 1 astronomical unit [AU]. This correction removes the $1/R^2$ effect due to the eccentricity of the Earth’s orbit. The 3% variation in the Sun–Earth distance produces a 6% change in irradiance.

Figure 13 shows an additional annual oscillation visible in the data products up to data processing Version 14. In addition to the $1/R^2$ effect, the apparent size of the Sun increases and decreases, thus exposing a slightly different area on the primary mirror. When the distance is smaller, the Sun illuminates some of the less-degraded parts of the optics, thus increasing the measured signal. Using the shape of the responsivity as a function of angle (Figure 5), we can estimate the magnitude of increased or decreased responsivity relative to the average. Removing this “second order” 1-AU correction produces the time series shown in red in Figure 13. Data versions from 15 onwards have this correction applied. The wavelength shown in Figure 13 was chosen because it has a very low solar variability, so the annual effect stands out. The solar-cycle variation at this wavelength is about 1.5% so a 0.1% correction is quite apparent. The solar-cycle trend in the V18 data product at this wavelength is not statistically significant, as discussed in Section 4. Figure 13 also clearly shows the six-month gap in the data in 2013 due to the spacecraft safe hold that led to the DO-Op mode of operation (Section 3.2).

4. Uncertainty Estimates

Estimating the uncertainty in SOLSTICE measurements is crucial to the scientific usefulness of the data record. Some sources of random uncertainty are very easy to estimate, such as the statistical uncertainty of a daily mean irradiance. The preflight systematic uncertainties

Figure 13 Example of a 1-nm time series from the MUV wavelength range showing the impact of the revised 1-AU correction. Without the revision, there was a distinct annual cycle. Note that this correction does not change the long-term degradation correction. The gap in observations for six months in 2013 is described in Section 3.2.

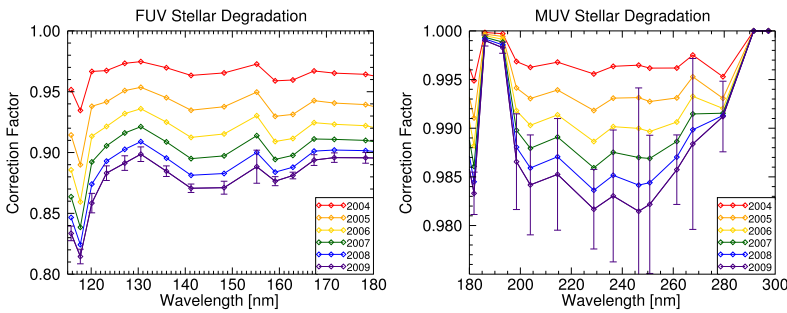
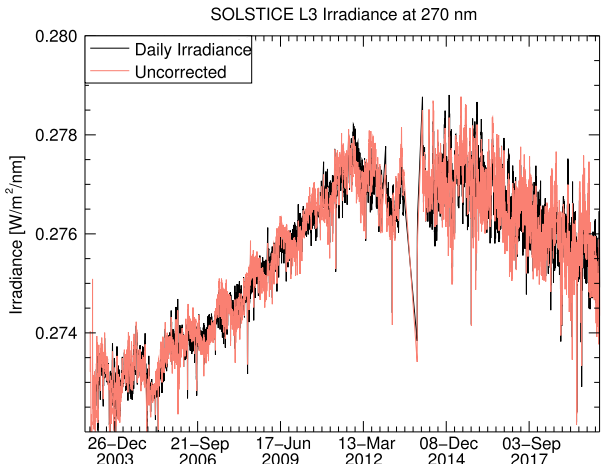


Figure 14 Degradation rates determined from stellar observations. The stars were observed from 2003 to 2009. The degradation as a function of wavelength at the end of each year are shown. Error bars are included only for the final year's curve for clarity.

were all carefully analyzed and documented by McClintock, Snow, and Woods (2005). The challenge is in estimating the uncertainty in the degradation correction as a function of both time and wavelength.

Figure 14 shows the degradation estimated by stellar measurements over the first six years of the SOLARIS mission. One curve per year is plotted, with the wavelengths where stellar irradiance is measured indicated by symbols. For clarity, the uncertainty of the curve is plotted as an error bars for the final year only. The curves are largely constant with wavelength, except for the shortest and longest. The stellar signals at these two extremes are low, so the correction for the dark-count rate is fractionally much larger. The systematic uncertainty at the long-wavelength end of the MUV is particularly difficult to estimate because of the low signal-to-noise ratio in both the solar and stellar measurements. The fits of the stellar-degradation curves show very little trend that is statistically significant. The redesign of the SOLSTICE instrument from its UARS predecessor did improve the MUV stellar signals with the removal of the neutral-density filters (McClintock, Rottman, and Woods, 2005), but the stellar signals were still too low to confidently detect a trend of about 1% over six years. The average fractional uncertainty in the stellar-degradation correction is 0.13% year⁻¹ in the FUV and 0.10% year⁻¹ in the MUV.

Table 1 Estimates of uncertainty in SOLSTICE degradation correction as a function of time for the MUV channel. The uncertainty in comparing any two SOLSTICE measurements depends on the time interval between them.

Component of degradation	Estimated trend uncertainty
Stellar correction	$\approx 0.1\% \text{ year}^{-1}$
FOV correction	$\approx 0.2\% \text{ year}^{-1}$
AB-Comparison correction (SOLSTICE A MUV Only)	$\approx 0.2\% \text{ year}^{-1}$
Combined uncertainty:	$\approx 0.3\% \text{ year}^{-1}$

Table 1 gives a summary of the sources of uncertainty in the SOLSTICE MUV long-term trend. The uncertainty in the degradation correction is determined by the uncertainty in the parameters of the exponential fits to the stellar and FOV observations. The MUV irradiances have an additional source of uncertainty from the cross-calibration of SOLSTICE B to SOLSTICE A due to an entrance-aperture anomaly (Snow et al., 2021). The formal uncertainty in these components yields a combined trend uncertainty of about 0.3% per year. The uncertainties are not strong functions of wavelength, so to first order they can be taken to be independent of wavelength. In the FUV, we apply only the stellar correction, which has a stability uncertainty of about 0.13% per year.

The correction for instrument and spacecraft anomalies described in the ATBD (Snow et al., 2021) add to the measurement uncertainty when comparing data before and after events. These additional uncertainties due to anomalies are included in the L3 data products. Stability uncertainty is not explicitly included in the L3 data files, since the uncertainty applies to comparisons made between two dates chosen by the user. Uncertainty in SSI variability $[E_1/E_2 - 1]$ would be the RSS of the measurement uncertainties for the two irradiances and the stability uncertainty. These three sources of error are independent, so they can be added in quadrature. The stability uncertainty is the dominant source of uncertainty for time periods longer than a year. The stability requirement for SOLSTICE in the original ATBD was 0.5% per year, so we meet this goal at all wavelengths.

5. Comparison to Other Datasets

One way of validating the SOLSTICE irradiance dataset is by comparison to independent SSI measurements. Some SSI datasets are cross-calibrated with SOLSTICE (e.g. Thiemann et al., 2019; Evans et al., 2010), so they do not allow validation of the SOLSTICE technique. Fortunately, there are a few simultaneous independent observations of SSI available for comparison of the MUV. In this section we show ratios on the absolute scale for two spacecraft. We also compare variability estimates for one broadband measurement and one empirical model.

5.1. PREMOS

The *PRECision Monitoring Sensor* (PREMOS: Cessateur et al., 2016) onboard the *Picard* mission (Thuillier et al., 2006) had several filter-radiometers to measure SSI. *Picard* operated from 2010 to 2014, so there is enough overlap in observations to compare long-term trends. Three of the wavelength bandpasses overlapped SOLSTICE: 210, 215, and 266 nm. The 215 nm channel had a FWHM of 10 nm, while the 210 and 266 nm channels had a wider FWHM of 20 nm. The PREMOS team was uncertain about degradation of their UV filters

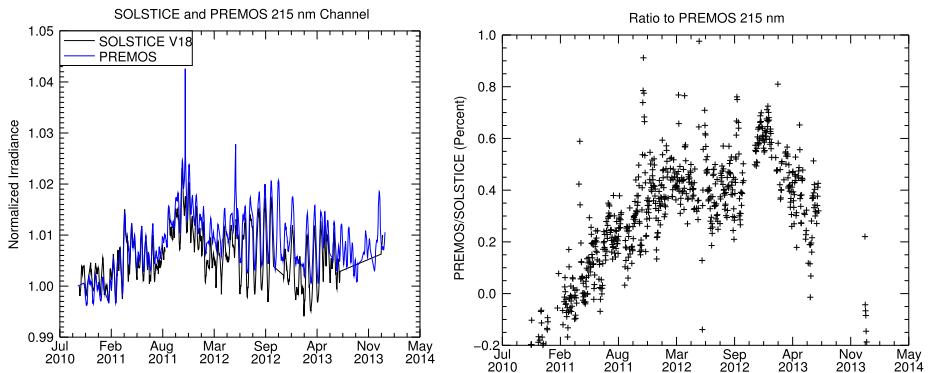


Figure 15 (left) Time series of normalized SSI from SOLSTICE and PREMOS at 215 nm. The SOLSTICE data were convolved with the PREMOS bandpass. (right) Ratio of the two time series in percent. The two time series agree to better than 1% over the course of the *Picard* mission.

prior to launch, so they adopted the SOLSTICE calibration for their absolute 215 scale (Schmutz et al., 2009; Cessateur et al., 2016). We have therefore normalized the two SSI datasets for comparison. We have convolved the 1 nm L3 Version 18 data product with the PREMOS bandpass. We have also taken the daily median value from the PREMOS dataset. Figure 15 (left) shows the normalized time series for the 215 nm channel and the SOLSTICE spectrum after convolution with the PREMOS bandpass. Solar variation on the rotational time scales are clearly visible and well matched in the two datasets.

The 215-nm channel used a backup detector head with a lower duty cycle to correct for long-term degradation. However, the 210- and 268-nm channels of PREMOS maintained their calibration relative to the 215-nm channel via correlation with the 215-nm observations and scaling by solar proxies (Cessateur et al., 2016). Therefore, these two channels do not provide independent validation of SOLSTICE long-term trending, and we limit comparisons to the 215-nm channel. Cessateur et al. (2016) compared SOLSTICE Versions 13 and 15 with PREMOS, and we update these comparisons here with the Version 18 SOLSTICE data.

The right panel of Figure 15 shows the ratio of SOLSTICE and PREMOS during the full PREMOS mission. There is a fairly linear increase in the PREMOS/SOLSTICE ratio of about 0.5% during the first year of overlap. The ratio becomes much flatter after that. There were no operational changes on SOLSTICE that might explain a difference in the trends starting in 2011. A change in the ratio after a *SORCE* battery anomaly at the end of 2012 (Woods et al., 2021) is visible (about 0.3%). The trend of the ratio after that could be an indication of a small change in the SOLSTICE calibration due to the spacecraft safehold (Woods et al., 2021) that is not adequately corrected in Version 18. The solar-cycle trends during the overlap with PREMOS have varied slightly between Versions 13, 15, and 18, but all agree better than 1%. This is consistent with the estimated uncertainty of the SOLSTICE long-term trend of $0.3\% \text{ year}^{-1}$.

5.2. ISS/SOLSPEC

Another independent measurement of UV SSI is from the *SOLAR SPECTrometer* (SOLSPEC: Thuillier et al., 2009) on the *International Space Station* (ISS). The instrument has a long design heritage dating back to 1983 (Labs et al., 1987). All references to SOLSPEC in this

article refer to the instrument that was flown on the ISS from 2008 to 2017. It is a three-channel grating spectrometer observing 165–3080 nm (Thuillier et al., 2009). Comparison to SOLSTICE uses the UV channel. It has a spectral resolution of 1.2 nm (Thuillier et al., 2009). SOLSPEC was calibrated before flight at the Physikalisch-Technische Bundesanstalt (PTB) blackbody (Sperfeld et al., 1995, 1998). Below 220 nm, the signal from the PTB blackbody source was too low, so deuterium lamps were used to calibrate SOLSPEC in the 165–200 nm range (Thuillier et al., 2009). The uncertainties for the first-light spectrum from SOLSPEC range from 1–2% in the UV channel (Thuillier et al., 2009).

A SOLSPEC first-light reference spectrum was constructed based on the first month of operation in April 2008. Meftah et al. (2016) published the results for three spectral bands: 165–180, 180–200, and 200–242 nm. They made comparisons to the Whole Heliosphere Interval (WHI) reference spectrum (Woods et al., 2009). They found a difference of 20% in the 165–180 nm band, $\approx 1\%$ in the 180–200 nm band, and about a 2% difference in 200–242 nm. The WHI spectrum in this wavelength range was created from SOLSTICE Version 9. Since the final data version for SOLSTICE is Version 18, it is worth revisiting the comparison.

Meftah et al. (2018, 2020) published updated versions of the SOLSPEC SSI spectrum. The SOLSPEC team has done a very detailed analysis of the sources of uncertainty as a function of wavelength in the UV (Bolsée et al., 2017; Meftah et al., 2018). Meftah et al. (2020) describe improvements to the SOLSPEC data-processing algorithms for the various wavelength ranges.

Figure 16 shows a comparison of SOLSTICE V18 to the SOLSPEC V2.0 spectrum. The black curve shows the ratio of the two spectra in April 2008. The SOLSPEC data were averaged over the entire month of April, while the SOLSTICE spectrum is the daily average for 5 April 2008. The Sun was very quiet during that month at solar minimum, so selecting any day in April would yield a similar result. The SOLSPEC team averaged over a month to increase the signal-to-noise ratio of that initial spectrum. The two spectra were smoothed to 1-nm resolution before taking the ratio. The red curves indicate the uncertainty envelope for the ratio. In this wavelength range, the SOLSTICE uncertainty is roughly 4% taking into account preflight uncertainty and five years of degradation uncertainty. The SOLSPEC uncertainty is from Meftah et al. (2020). The two uncertainties are independent above 180 nm, so they can be added in quadrature.

It should be noted that Meftah et al. (2020) do not provide an uncertainty for wavelengths below 180 nm because the authors recalibrated their spectrum in this wavelength range to match SOLSTICE. So, the combined uncertainty is just the 4% SOLSTICE uncertainty for 165–180 nm. For longer wavelengths, the two spectra agree within their $1\text{-}\sigma$ uncertainties.

5.3. TSIS-1 and SORCE SIM

Two additional instruments made overlapping measurements with SOLSTICE. There is a *Spectral Irradiance Monitor* (SIM) onboard SORCE (Harder et al., 2005) and a similar instrument on the *Total and Spectral Irradiance Sensors-1* (TSIS-1) mission onboard the ISS (Richard et al., 2020). These two instruments are prism spectrometers with many shared design elements, so the comparisons with both instruments are merged into a single section here.

Both instruments use cycling between redundant channels to monitor long-term degradation. SORCE/SIM has only two redundant channels, while TSIS-1/SIM has three. Both instruments overlap with SOLSTICE in the MUV wavelength range. SORCE/SIM's accurate measurement range includes 240–310 nm, while TSIS-1/SIM extends this range down to 200 nm.

Figure 16 Ratio of SOLSPEC V2.0 spectrum to SOLSTICE V18 for April 2008. The *black curve* shows the ratio of the two spectra, and the *red curves* show the upper and lower $1\text{-}\sigma$ uncertainty bounds for the ratio. The 165–180 nm range has been rescaled to match SOLSTICE (Meftah et al., 2020) so that the ratio is unity and the uncertainty is due to SOLSTICE alone.

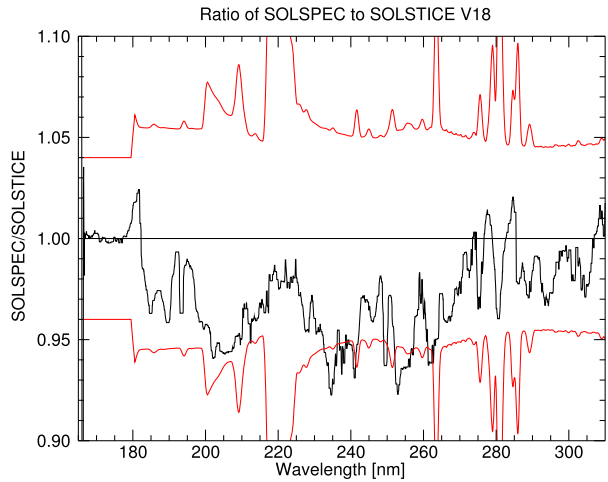


Figure 17 Ratio of TSIS-1/SIM (blue) and SORCE/SIM (red) to SOLSTICE for 1 April 2018. The uncertainty in the stability of SOLSTICE after fifteen years in orbit is about $\pm 5\%$, so this ratio is within the $1\text{-}\sigma$ error band.

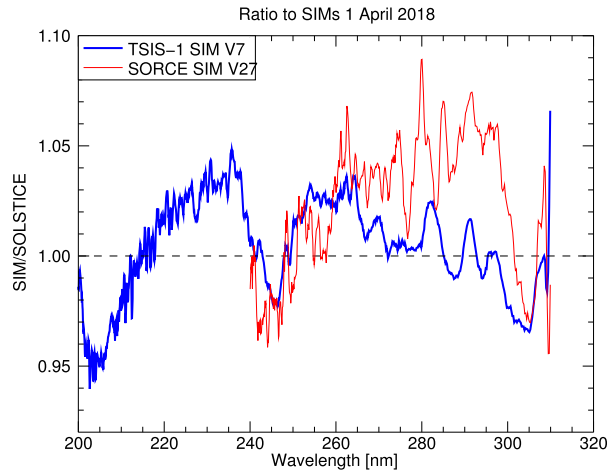


Figure 17 shows the ratio of SOLSTICE observations on 1 April 2018 to those from TSIS-1 and SORCE SIM. This date was chosen near the beginning of TSIS-1 operations, when little degradation was expected. The L3 high-resolution SOLSTICE spectrum was convolved with the SIM instrument profile using the IDL procedure on the TSIS-1 web page: lasp.colorado.edu/home/tsis/data/ssi-data/. The agreement is well within the uncertainty of the SOLSTICE stability. Recall that this comparison is fifteen years into the SORCE mission, and the SOLSTICE trend uncertainty alone is $0.3\% \text{ year}^{-1}$. Therefore the $1\text{-}\sigma$ uncertainty for SOLSTICE alone is about 5%.

The analysis of the detailed wavelength structure of this comparison will be part of an ongoing SIST-3 project. The upward trend from 200–240 nm and the down-up shape from 240–270 nm in the ratio have corresponding shapes in Figure 9. It is certainly suggestive of a systematic error in the SOLSTICE FOV correction, and it will also be investigated by NASA's Solar Irradiance Science Team-3 (SIST-3) program.

The comparison to SORCE/SIM is also a validation of the SIM degradation model in the UV. This ratio was not normalized. It is the ratio of the public V27 SIM to V18 SOLSTICE.

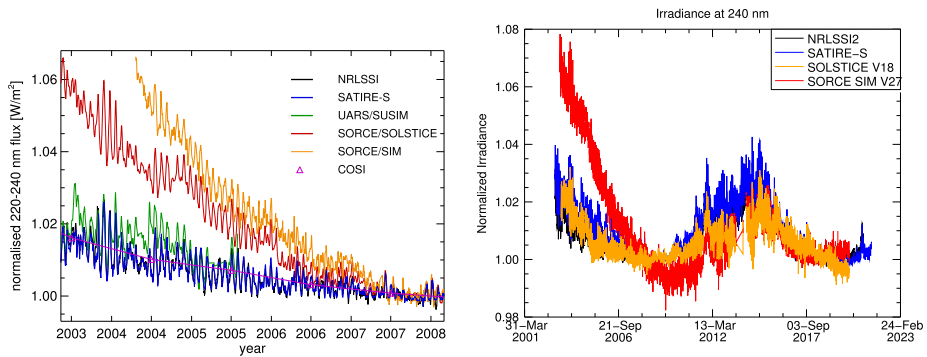


Figure 18 (left) Reproduction of Figure 8 from Ermolli et al. (2013) showing SOLSTICE Version 13 for comparison. Time series of irradiances were normalized to the minimum of Solar Cycles 23/24. (right) Time series of irradiances normalized to 1 April 2018 using the latest versions of SOLSTICE (V18) and SIM (V27). Figure is reproduced with permission of the author.

Although the SIM and SOLSTICE teams work together on understanding spacecraft issues, the two data products are produced by completely independent algorithms.

5.4. Irradiance Models

Throughout the SOLSTICE mission, there have been many articles about the solar-cycle behavior of the SSI measurements. A subset of the articles concentrating on the UV include: Haigh et al. (2010), Ball et al. (2011), Deland and Cebula (2012), Unruh, Ball, and Krivova (2012), Morrill, Floyd, and McMullin (2014), Woods et al. (2018, 2022). At the end of Solar Cycle 23, Ermolli et al. (2013) published an overview of the issues regarding the observed trends in the SOLSTICE and SIM SSI data products. The decline of Solar Cycle 23 in the data versions at that time showed a much larger variation than had been seen in the data from previous solar cycles and was not consistent with the correlations to solar proxies that had been developed prior to SOLSTICE. Figure 18 shows a comparison of the SOLSTICE SSI measurements to the SATIRE-S (Yeo et al., 2014) and NRLSSI (Coddington et al., 2016) models. The left panel is the summary plot from Ermolli et al. (2013). In this figure, the time series are all normalized to the solar minimum in 2008. Both SIM and SOLSTICE show a much larger variation than the models or SUSIM observations. The differences were much larger than the quoted uncertainties for the SOLSTICE measurements.

Over the next several years, the SOLSTICE team continued to analyze calibration data and developed new algorithms to correct the irradiances for degradation as described in Section 3.2. The results at the end of the SOLSTICE mission are summarized for one wavelength in the right panel of Figure 18. In this figure, all of the time series are normalized to 1 April 2018. For SOLSTICE, there is now reasonable agreement with the models for both Solar Cycles 23 and 24. The SIM data in Cycle 24 at this wavelength also match model estimates. The details of the SIM degradation analysis are beyond the scope of this article; see Harder et al. (2022). We include the SIM data only for comparison. Further analysis of both SIM and SOLSTICE continues through a SIST-3 project.

Long-term monitoring of UV SSI by SOLSTICE has included more than one solar cycle. Woods et al. (2022) discuss the solar-cycle results for all the SOLSTICE instruments, so we provide a summary for only SOLSTICE here. Figure 18 showed the time series for a 1-nm subset of the SOLSTICE data. It is an important wavelength for atmospheric studies, but it

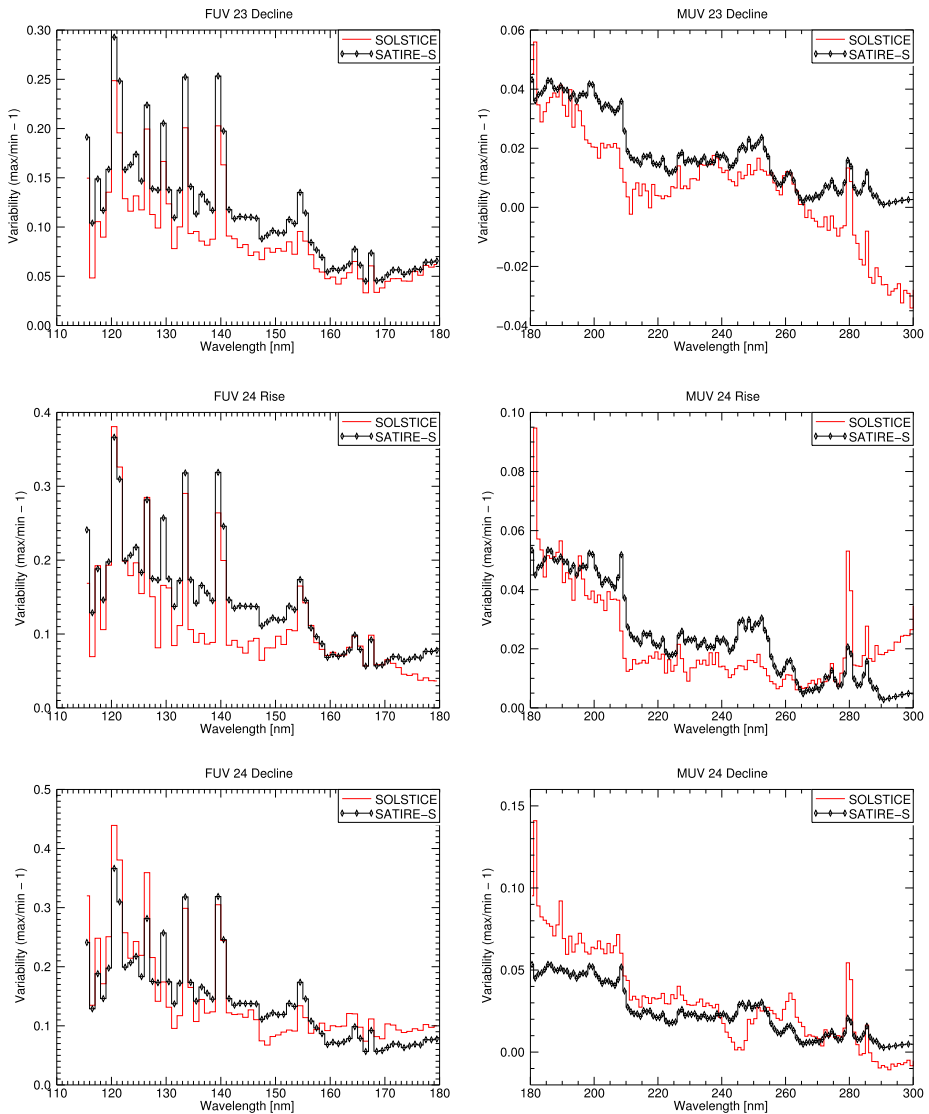


Figure 19 Solar-cycle variability as a function of wavelength for SOLSTICE (V18). The results from SATIRE-S are also shown to provide context to the SOLSTICE measurements.

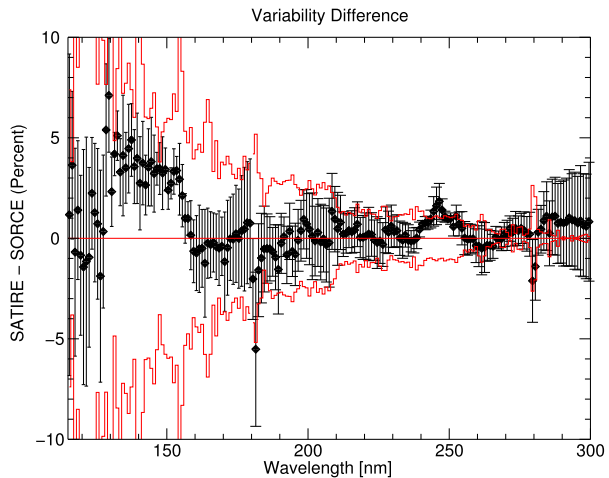
is useful to look at the entire spectral range measured by SOLSTICE as well. We define the variability between two dates as the ratio of the irradiances minus one, i.e. $(E_2/E_1) - 1$. The variability as a function of wavelength for SOLSTICE V18 is shown in Figure 19.

The dates used to define the solar maximum and minimum are shown in Table 2. As discussed by Woods et al. (2022), solar-maximum and -minimum periods extend over a wide range of time and there are many criteria that can be used to define them. Minimum and maximum dates can also be functions of wavelength (White et al., 2011), but we have chosen a single date for all wavelengths for simplicity. These dates are the same as those adopted by Woods et al. (2022). It should be noted that SOLSTICE did not begin observations until

Table 2 Dates of solar-cycle minimum and maximum. See text for explanation of SORCE's Cycle 23 maximum. The dates were chosen to align with Woods et al. (2022).

Solar Cycle	Feature	Date [YYYY/DOY]
23	Maximum (SORCE)	2004/234
23/24	Minimum	2008/315
24	Maximum	2011/351
24/25	Minimum	2019/289

Figure 20 Mean difference in variability between SOLSTICE and SATIRE-S for the three time periods shown in Figure 19 in percent as a function of wavelength. The red curves are the envelope of rotational variability (5–18 July 2005) for comparison (see text).



well after the peak of Solar Cycle 23. The date in mid-2004 was chosen in order to include measurements from all the SORCE instruments. SORCE/SIM did not start publishing L3 data until April 2004, and the chosen date corresponds to a peak in the 81-day averaged Mg II index after that. The Cycle 23/24 minimum agrees with the value published by White et al. (2011). Cycle 24 had several peaks, and Woods et al. (2022) chose the earliest in order to avoid the gap in SORCE observations caused by the spacecraft emergency in 2013. The Cycle 24/25 minimum is the commonly accepted date: www.swpc.noaa.gov/news/solar-prediction-scientists-announce-solar-cycle-25.

The variability of SATIRE-S (Yeo et al., 2014) for the same time ranges is also shown in each panel of Figure 19 for context. In order to simplify the plots, we have included only one model. SATIRE-S was chosen because it is the most independent from the SOLSTICE dataset. NRLSSI (Coddington et al., 2016) uses SOLSTICE data in deriving its parameters in this wavelength range.

Figure 20 shows the average difference between the SOLSTICE variability and the SATIRE-S variability for the three time periods in percentage. The standard deviation of the three differences is also shown. While there are regions of systematic differences, in general the V18 SOLSTICE solar-cycle variability agrees with the variability estimated from SATIRE-S. The SC23 decline is a period of about four years, so the estimated uncertainty of the SOLSTICE degradation over this interval is about 1%. Similarly, the SC24 rise is about three years, again about a 1% uncertainty in the SOLSTICE variability. The decline of SC24 was much more prolonged in this dataset and included the correction for the spacecraft emergency in 2013, so its uncertainty is closer to 4%. On average, the variability measured by SOLSTICE agrees with SATIRE-S to within this uncertainty at most

wavelengths. For context, Figure 20 also includes the variation of SOLSTICE irradiance as a function of wavelength for one rotation: 5–18 July 2005 (red curves). This time period was chosen as a typical example of a rotation. The shape is similar for all rotations, but the magnitude can vary. The purpose of including an average rotation is to give an indication of the statistical significance of the comparison to SATIRE-S. The standard deviation of the difference in variability for wavelengths longer than 260 nm is larger than the variability that we are trying to measure (except for the strong variation of the Mg II h and k lines at 280 nm). In contrast, the standard deviation of the difference at Lyman α is much smaller than the solar-cycle variation at 121.5 nm. Woods et al. (2022) provide more detailed discussions about SSI variability and additional comparisons to other models and SSI composites.

6. Discussion

The goals of this article are twofold: First, to describe the methods and algorithms used in processing the SOLSTICE spacecraft data. Over the long SORCE mission, there were many changes to the analysis. Some were mandated by operational constraints such as aperture anomalies and battery degradation. Others were upgrades to the originally planned algorithms such as wavelength determination and the SAA.

The preflight requirements on absolute calibration and stability over time were designed to measure expected variation over the solar cycle. The calibration observations of stars, the FOV, the wavelength scale, etc. were all designed to meet these requirements. The elements of the measurement equation that were tracked by the calibration observations were all maintained to assure that the stability requirement was met. However, the solar-cycle variability at wavelengths longer than 260 nm is smaller than the uncertainty in the stability. The requirement on SOLSTICE stability was better than 0.5% per year, and we achieved close to 0.3% per year. But a solar-cycle variability of less than 2% at wavelengths above 260 nm falls within that uncertainty over half a solar-cycle (i.e. five years).

The second main goal of this article is to show the results of these algorithm changes when SOLSTICE is compared to other datasets and models. During much of the SORCE mission, the public data products showed long-term trends that exceeded expectations for solar-cycle variation, especially in the MUV wavelength range. Version 18 data products, which implement all of the algorithm changes described in this manuscript, show much better agreement with models and independent measurements than shown by earlier data versions.

In the MUV, the best-calibrated independent measurement is the TSIS-1/SIM (Richard et al., 2020). Fifteen years into the SORCE mission, the MUV SSI from 200–310 nm from SOLSTICE agrees with TSIS-1/SIM to better than $\pm 5\%$. That is in line with our estimate of about 0.3% per year uncertainty in the degradation correction.

The comparison to ISS/SOLSPEC midway through the SORCE mission at solar minimum was also consistent with the combined uncertainties of the two measurements. The SOLSPEC uncertainty is a complex function of wavelength (Meftah et al., 2020), so it is impossible to interpret specific features of the ratio in terms of one instrument or another. However, the ratio shown in Figure 16 does provide validation of the calibration and stability estimates for both instruments.

Woods et al. (2022) describe the solar-cycle behavior of the SORCE instruments in more detail. The main conclusion of that article is that the trends observed by SORCE during Cycle 24 are much more in line with predictions and models. The Solar Cycle 23 trends in the end-of-mission data products are still larger than expected at many wavelengths, particularly

for $\lambda > 260$ nm. Figure 19 would seem to show reasonable agreement with the SATIRE-S model, but the uncertainty in the SOLSTICE measurements above 260 nm is larger than the variability due to the solar cycle.

These comparisons of SOLSTICE solar observations validate the SOLSTICE technique of using the same optics for both solar and stellar measurements. The SOLSTICE technique has been successfully used for over 30 years onboard the UARS and SORCE spacecraft. The on-going and future observations of solar UV irradiance by TSIS/SIM and GOES/EXIS do not use the SOLSTICE technique. CSOL, which will fly on *INSPIRESat3*, does not observe stars, so it will not use the SOLSTICE technique. It is not clear when the SOLSTICE technique will be applied next to extend solar-irradiance climate record for the FUV and MUV range. There is currently a spectral gap in the 140 nm to 200 nm range for UV SSI measurements, so there is good potential to apply the SOLSTICE technique again in the near future to address this spectral gap.

Acknowledgments This work was supported by NASA contract NAS5-97045 to the University of Colorado Boulder and the South African National Research Foundation (Grant Number 132800). The SORCE/SOLSTICE analysis team at LASP has had contributions from many people over the long mission, not just those on the author list. The SOLSTICE team would like to thank Stéphane Béland, Ken Greist, Emma Lieb, Doug Lindholm, Deb McCabe, Gary Rottman, Chris Pankratz, Steve Penton, Blake Vanier, Don Woodraska, and especially Vanessa George. M. Snow now would also like to acknowledge the support that the SORCE project provided for many undergraduate research assistants. Some of the results included here were based on the research results of those REU projects: Julie Feldt, James McGrail, Paige Bailey, Erica Dolinar, Laura O'Connor, Ariana Giorgi, Willow Reed, Zoe Pierrat, and Austin Ortiz.

Data Availability All of the SORCE data products shown here are available through the SORCE web page lasp.colorado.edu/sorce or the LASP Interactive Solar Irradiance Datacenter (LISIRD) lasp.colorado.edu/lisird.

Declarations

Disclosure of Potential Conflicts of Interest The authors declare that they have no conflicts of interest.

Open Access This article is licensed under a Creative Commons Attribution 4.0 International License, which permits use, sharing, adaptation, distribution and reproduction in any medium or format, as long as you give appropriate credit to the original author(s) and the source, provide a link to the Creative Commons licence, and indicate if changes were made. The images or other third party material in this article are included in the article's Creative Commons licence, unless indicated otherwise in a credit line to the material. If material is not included in the article's Creative Commons licence and your intended use is not permitted by statutory regulation or exceeds the permitted use, you will need to obtain permission directly from the copyright holder. To view a copy of this licence, visit <http://creativecommons.org/licenses/by/4.0/>.

References

- Arp, U., Friedman, R., Furst, M.L., Makar, S., Shaw, P.-S.: 2000, SURF III – an improved storage ring for radiometry. *Metrologia* **37**, 357. DOI. ADS.
- Ball, W.T., Unruh, Y.C., Krivova, N.A., Solanki, S., Harder, J.W.: 2011, Solar irradiance variability: a six-year comparison between SORCE observations and the SATIRE model. *Astron. Astrophys.* **530**, A71. DOI. ADS.
- Bolsée, D., Pereira, N., Gillotay, D., Pandey, P., Cessateur, G., Foujols, T., Bekki, S., Hauchecorne, A., Mef-tah, M., Damé, L., Hersé, M., Michel, A., Jacobs, C., Sela, A.: 2017, SOLAR/SOLSPEC mission on ISS: in-flight performance for SSI measurements in the UV. *Astron. Astrophys.* **600**, A21. DOI. ADS.
- Cessateur, G., Schmutz, W., Wehrli, C., Gröbner, J., Haberleiter, M., Kretschmar, M., Rozanov, E., Schöll, M., Shapiro, A., Thuillier, G., Egorova, T., Finsterle, W., Fox, N., Hochedez, J.-F., Koller, S., Mef-tah, M., Meindl, P., Nyeki, S., Pfiffner, D., Roth, H., Rouzé, M., Spescha, M., Tagirov, R., Werner, L., Wyss, J.-U.: 2016, Solar irradiance observations with PREMOS filter radiometers on the PICARD mission: in-flight performance and data release. *Astron. Astrophys.* **588**, A126. DOI. ADS.

- Chaffin, M.S., Chaufray, J.Y., Deighan, J., Schneider, N.M., Mayyasi, M., Clarke, J.T., Thiemann, E., Jain, S.K., Crismani, M.M.J., Stiepen, A., Eparvier, F.G., McClintock, W.E., Stewart, A.I.F., Holsclaw, G.M., Montmessin, F., Jakosky, B.M.: 2018, Mars H escape rates derived from MAVEN/IUVS Lyman alpha brightness measurements and their dependence on model assumptions. *J. Geophys. Res.* **123**, 2192. DOI. ADS.
- Chamberlin, P.C., Eparvier, F.G., Knoer, V., Leise, H., Pankratz, A., Snow, M., Templeman, B., Thiemann, E.M.B., Woodraska, D.L., Woods, T.N.: 2020, The Flare Irradiance Spectral Model-Version 2 (FISM2). *Space Weather* **18**, e02588. DOI. ADS.
- Coddington, O., Lean, J.L., Pilewskie, P., Snow, M., Lindholm, D.: 2016, A solar irradiance climate data record. *Bull. Am. Meteorol. Soc.* **97**, 1265. DOI. ADS.
- Cunningham, N.J., Spencer, J.R., Feldman, P.D., Strobel, D.F., France, K., Osterman, S.N.: 2015, Detection of Callisto's oxygen atmosphere with the Hubble Space Telescope. *Icarus* **254**, 178. DOI. ADS.
- Deland, M.T., Cebula, R.P.: 2012, Solar UV variations during the decline of Cycle 23. *J. Atmos. Solar-Terr. Phys.* **77**, 225. DOI. ADS.
- Ermolli, I., Matthes, K., Dudok de Wit, T., Krivova, N.A., Tourpali, K., Weber, M., Unruh, Y.C., Gray, L., Langematz, U., Pilewskie, P., Rozanov, E., Schmutz, W., Shapiro, A., Solanki, S.K., Woods, T.N.: 2013, Recent variability of the solar spectral irradiance and its impact on climate modelling. *Atmos. Chem. Phys.* **13**, 3945. DOI. ADS.
- Evans, J.S., Strickland, D.J., Woo, W.K., McMullin, D.R., Plunkett, S.P., Viereck, R.A., Hill, S.M., Woods, T.N., Eparvier, F.G.: 2010, Early observations by the GOES-13 Solar Extreme Ultraviolet Sensor (EUVS). *Solar Phys.* **262**, 71. DOI. ADS.
- Gröller, H., Montmessin, F., Yelle, R.V., Lefèvre, F., Forget, F., Schneider, N.M., Koskinen, T.T., Deighan, J., Jain, S.K.: 2018, MAVEN/IUVS stellar occultation measurements of Mars atmospheric structure and composition. *J. Geophys. Res.* **123**, 1449. DOI. ADS.
- Haigh, J.D.: 1994, The role of stratospheric ozone in modulating the solar radiative forcing of climate. *Nature* **370**, 544. DOI. ADS.
- Haigh, J.D., Winning, A.R., Toumi, R., Harder, J.W.: 2010, An influence of solar spectral variations on radiative forcing of climate. *Nature* **467**, 696. DOI. ADS.
- Harder, J., Lawrence, G., Fontenla, J., Rottman, G., Woods, T.: 2005, The spectral irradiance monitor: scientific requirements, instrument design, and operation modes. *Solar Phys.* **230**, 141. DOI. ADS.
- Harder, J.W., Béland, S., Penton, S., Woods, T.N.: 2022, Long-term Trend Analysis in the SORCE Spectral Irradiance Monitor. *Solar Phys.*, accepted.
- Heath, D.F., Schlesinger, B.M.: 1986, The Mg 280-nm doublet as a monitor of changes in solar ultraviolet irradiance. *J. Geophys. Res.* **91**, 8672. DOI. ADS.
- Jessup, K.L., Marcq, E., Mills, F., Mahieux, A., Limaye, S., Wilson, C., Allen, M., Bertaux, J.-L., Markiewicz, W., Roman, T., Vandaele, A.-C., Wilquet, V., Yung, Y.: 2015, Coordinated Hubble Space Telescope and Venus express observations of Venus' upper cloud deck. *Icarus* **258**, 309. DOI. ADS.
- Jessup, K.-L., Marcq, E., Bertaux, J.-L., Mills, F.P., Limaye, S., Roman, A.: 2020, On Venus' cloud top chemistry, convective activity and topography: a perspective from HST. *Icarus* **335**, 113372. DOI. ADS.
- Kren, A.C., Pilewskie, P., Coddington, O.: 2017, Where does Earth's atmosphere get its energy? *J. Space Weather Space Clim.* **7**, A10. DOI. ADS.
- Kretschmar, M., Snow, M., Curdt, W.: 2018, An empirical model of the variation of the solar Lyman- α spectral irradiance. *Geophys. Res. Lett.* **45**, 2138. DOI. ADS.
- Labs, D., Neckel, H., Simon, P.C., Thuillier, G.: 1987, Ultraviolet solar irradiance measurement from 200-NM to 358-NM during SPACELAB-1 mission. *Solar Phys.* **107**, 203. DOI. ADS.
- Machol, J.L., Eparvier, F.G., Viereck, R.A., Woodraska, D.L., Snow, M., Thiemann, E., Woods, T.N., McClintock, W.E., Mueller, S., Eden, T.D., Meisner, R., Codrescu, S., Bouwer, S.D., Reinard, A.A.: 2020, Chapter 19 - GOES-R series solar X-ray and ultraviolet irradiance. In: Goodman, S.J., Schmit, T.J., Daniels, J., Redmon, R.J. (eds.) *The GOES-R Series*, Elsevier, Amsterdam, 233. ISBN 978-0-12-814327-8. DOI.
- Markwardt, C.B.: 2009, Non-linear least-squares fitting in IDL with MPFIT. In: Bohlender, D.A., Durand, D., Dowler, P. (eds.) *Astronomical Data Analysis Software and Systems XVIII CS-411*, Astron. Soc. Pacific, San Francisco, 251. ADS.
- McClintock, W.E., Rottman, G.J., Woods, T.N.: 2005, Solar-stellar irradiance comparison experiment II (Solstice II): instrument concept and design. *Solar Phys.* **230**, 225. DOI. ADS.
- McClintock, W.E., Snow, M., Woods, T.N.: 2005, Solar-stellar irradiance comparison experiment II (SOLSTICE II): pre-launch and on-orbit calibrations. *Solar Phys.* **230**, 259. DOI. ADS.
- Meftah, M., Bolsée, D., Damé, L., Hauchecorne, A., Pereira, N., Irbah, A., Bekki, S., Cessateur, G., Foujols, T., Thiéblemont, R.: 2016, Solar irradiance from 165 to 400 nm in 2008 and UV variations in three spectral bands during solar cycle 24. *Solar Phys.* **291**, 3527. DOI. ADS.

- Meftah, M., Damé, L., Bolsée, D., Hauchecorne, A., Pereira, N., Sluse, D., Cessateur, G., Irbah, A., Bureau, J., Weber, M., Bramstedt, K., Hilbig, T., Thiéblemont, R., Marchand, M., Lefèvre, F., Sarkissian, A., Bekki, S.: 2018, SOLAR-ISS: a new reference spectrum based on SOLAR/SOLSPEC observations. *Astron. Astrophys.* **611**, A1. DOI ADS.
- Meftah, M., Damé, L., Bolsée, D., Pereira, N., Snow, M., Weber, M., Bramstedt, K., Hilbig, T., Cessateur, G., Boudjella, M.-Y., Marchand, M., Lefèvre, F., Thiéblemont, R., Sarkissian, A., Hauchecorne, A., Keckhut, P., Bekki, S.: 2020, A new version of the SOLAR-ISS spectrum covering the 165–3000 nm spectral region. *Solar Phys.* **295**, 14. DOI ADS.
- Mihalas, D., Binney, J.: 1981, *Galactic Astronomy. Structure and Kinematics*, Freeman, New York. ADS.
- Milligan, R.O., Chamberlin, P.C.: 2016, Anomalous temporal behaviour of broadband Ly α observations during solar flares from SDO/EVE. *Astron. Astrophys.* **587**, A123. DOI ADS.
- Molyneux, P.M., Nichols, J.D., Becker, T.M., Raut, U., Retherford, K.D.: 2020, Ganymede's far-ultraviolet reflectance: constraining impurities in the surface ice. *J. Geophys. Res.* **125**, e06476. DOI ADS.
- Morrill, J.S., Floyd, L., McMullin, D.: 2014, Comparison of solar UV spectral irradiance from SUSIM and SORCE. *Solar Phys.* **289**, 3641. DOI ADS.
- O'Connor, L.J., Snow, M.A.: 2011, The location and evolution of the South Atlantic Anomaly as observed by SOLSTICE. In: *AGU Fall Meeting Abs*, SM51C. ADS.
- Pauluhn, A., Huber, M.C.E., Smith, P.L., Colina, L.: 2015, Spectroradiometry with space telescopes. *Astron. Astrophys. Rev.* **24**, 3. DOI ADS.
- Pavón-Carrasco, F.J., De Santis, A.: 2016, The South Atlantic Anomaly: the key for a possible geomagnetic reversal. *Front. Earth Sci.* **4**, 40. DOI ADS.
- Pierrat, Z., Snow, M.A., Machol, J.L.: 2016, Estimating exospheric hydrogen density using Lyman- α solar irradiance measurements from SOLSTICE. In: *AGU Fall Meeting Abs*, SA51B. ADS.
- Pryor, W.R., Snow, M., Quémerais, E., Ferron, S.: 2013, Lyman- α observations of comet Holmes from SORCE SOLSTICE and SOHO SWAN. In: Quémerais, E., Snow, M., Bonnet, R.-M. (eds.) *Cross-Calibration of Far UV Spectra of Solar System Objects and the Heliosphere, ISSI Scientific Report Series 13*, Springer, New York, 255. DOI ADS.
- Richard, E., Harber, D., Coddington, O., Drake, G., Rutkowski, J., Triplett, M., Pilewskie, P., Woods, T.: 2020, SI-traceable spectral irradiance radiometric characterization and absolute calibration of the TSIS-1 Spectral Irradiance Monitor (SIM). *Remote Sens.* **12**, 1818. DOI ADS.
- Roth, L., Ivchenko, N., Gladstone, G.R., Saur, J., Grodent, D., Bonfond, B., Molyneux, P.M., Retherford, K.D.: 2021, A sublimated water atmosphere on Ganymede detected from Hubble Space Telescope observations. *Nat. Astron.* **5**, 1043. DOI ADS.
- Rottman, G.: 2005, The SORCE mission. *Solar Phys.* **230**, 7. DOI ADS.
- Rottman, G.J., Woods, T.N., Sparn, T.P.: 1993, Solar-stellar irradiance comparison experiment I. I – Instrument design and operation. *J. Geophys. Res.* **98**, 10,667. DOI ADS.
- Rottman, G., Woods, T., Snow, M., DeToma, G.: 2001, The solar cycle variation in ultraviolet irradiance. *Adv. Space Res.* **27**, 1927. DOI ADS.
- Schmutz, W., Fehlmann, A., Hülsen, G., Meindl, P., Winkler, R., Thuillier, G., Blattner, P., Buisson, F., Egorova, T., Finsterle, W., Fox, N., Gröbner, J., Hochedez, J.-F., Koller, S., Meftah, M., Meissonnier, M., Nyeki, S., Pfiffner, D., Roth, H., Rozanov, E., Spescha, M., Wehrli, C., Werner, L., Wyss, J.U.: 2009, The PREMOS/PICARD instrument calibration. *Metrologia* **46**, S202. DOI ADS.
- Snow, M., Elliott, J.P.: 2021, SORCE Solar Stellar Irradiance Comparison Experiment (SOLSTICE) release notes. Technical report, University of Colorado Boulder. DOI.
- Snow, M., McClintock, W.E.: 2005, High time cadence solar magnesium II index monitor. In: Fineschi, S., Viereck, R.A. (eds.) *Solar Physics and Space Weather Instrumentation, Soc. Photo-Opt. Instrum. Eng. (SPIE) CS-5901*, 354. DOI ADS.
- Snow, M., McClintock, W.E., Rottman, G., Woods, T.N.: 2005a, Solar stellar irradiance comparison experiment II (Solstice II): examination of the solar stellar comparison technique. *Solar Phys.* **230**, 295. DOI ADS.
- Snow, M., McClintock, W.E., Woods, T.N., White, O.R., Harder, J.W., Rottman, G.: 2005b, The Mg II index from SORCE. *Solar Phys.* **230**, 325. DOI ADS.
- Snow, M., McClintock, W.E., Crotser, D., Eparvier, F.G.: 2009, EUVS-C: the measurement of the magnesium II index for GOES-R EXIS. In: Fineschi, S., Fennelly, J.A. (eds.) *Solar Physics and Space Weather Instrumentation III, Soc. Photo-Opt. Instrum. Eng. (SPIE) CS-7438*, 743803. DOI ADS.
- Snow, M., Reberac, A., Quémerais, E., Clarke, J., McClintock, W.E., Woods, T.N.: 2013a, A new catalog of ultraviolet stellar spectra for calibration. In: Quémerais, E., Snow, M., Bonnet, R.-M. (eds.) *Cross-Calibration of Far UV Spectra of Solar System Objects and the Heliosphere, ISSI Scientific Report Series 13*, Springer, New York, 191. DOI ADS.
- Snow, M., Holsclaw, G.M., McClintock, W.E., Woods, T.: 2013b, Absolute ultraviolet irradiance of the Moon from the LASP lunar albedo measurement and analysis from SOLSTICE (LLAMAS) project.

- In: Quémerais, E., Snow, M., Bonnet, R.-M. (eds.) *Cross-Calibration of Far UV Spectra of Solar System Objects and the Heliosphere, ISSI Scientific Report Series 13*, Springer, New York, 227. DOI. ADS.
- Snow, M., McClintock, W.E., Elliott, J.P., Vanier, B., Lieb, E., George, V.: 2021, Algorithm Theoretical Basis Document – Post Launch update: Solar Stellar Irradiance Comparison Experiment (SOLSTICE). Technical report, University of Colorado Boulder. DOI.
- Sperfeld, P., Raatz, K.-H., Nawo, B., Müller, W., Metzdorf, J.: 1995, Spectral-irradiance scale based on radiometric black-body temperature measurements. *Metrologia* **32**, 435. DOI. ADS.
- Sperfeld, P., Metzdorf, J., Galal Yousef, S., Stock, K.D., Möller, W.: 1998, Improvement and extension of the black-body-based spectral irradiance scale. *Metrologia* **35**, 267. DOI. ADS.
- Stephens, G.L., Li, J., Wild, M., Clayson, C.A., Loeb, N., Kato, S., L'Ecuyer, T., Stackhouse, P.W., Lebsock, M., Andrews, T.: 2012, An update on Earth's energy balance in light of the latest global observations. *Nat. Geosci.* **5**, 691. DOI. ADS.
- Taylor, B.N., Kyuatt, C.E.: 2001, Guidelines for evaluating and expressing the uncertainty of NIST measurement results. Technical Report 1297, National Institute of Standards and Technology, Gaithersburg, MD.
- Thiemann, E.M.B., Eparvier, F.G., Woodraska, D., Chamberlin, P.C., Machol, J., Eden, T., Jones, A.R., Meisner, R., Mueller, S., Snow, M., Viereck, R., Woods, T.N.: 2019, The GOES-R EUVS model for EUV irradiance variability. *J. Space Weather Space Clim.* **9**, A43. DOI. ADS.
- Thiemann, E., Harder, J., Woods, T.N., Snow, M., Klapetzky, M., Triplett, M., Sims, A., Penton, S.: 2022, FUV solar irradiance spectra from the Compact SOLSTICE rocket experiment. *Solar Phys.*, submitted.
- Thuillier, G., Dewitte, S., Schmutz, W., Picard Team: 2006, Simultaneous measurement of the total solar irradiance and solar diameter by the PICARD mission. *Adv. Space Res.* **38**, 1792. DOI. ADS.
- Thuillier, G., Foujols, T., Bolsée, D., Gillotay, D., Hersé, M., Peetermans, W., Decuyper, W., Mandel, H., Sperfeld, P., Pape, S., Taubert, D.R., Hartmann, J.: 2009, SOLAR/SOLSPEC: scientific objectives, instrument performance and its absolute calibration using a blackbody as primary standard source. *Solar Phys.* **257**, 185. DOI. ADS.
- Unruh, Y.C., Ball, W.T., Krivova, N.A.: 2012, Solar irradiance models and measurements: a comparison in the 220–240 nm wavelength band. *Surv. Geophys.* **33**, 475. DOI. ADS.
- White, O., Kopp, G., Snow, M., Tapping, K.: 2011, The solar cycle 23–24 minimum. A benchmark in solar variability and effects in the heliosphere. *Solar Phys.* **274**, 159. DOI. ADS.
- Woods, T.N., DeLand, M.T.: 2021, An improved solar spectral irradiance composite record. *Earth Space Sci.* **8**, e01740. DOI. ADS.
- Woods, T.N., Eparvier, F.G., Fontenla, J., Harder, J., Kopp, G., McClintock, W.E., Rottman, G., Smiley, B., Snow, M.: 2004, Solar irradiance variability during the October 2003 solar storm period. *Geophys. Res. Lett.* **31**, L10802. DOI. ADS.
- Woods, T.N., Chamberlin, P.C., Harder, J.W., Hock, R.A., Snow, M., Eparvier, F.G., Fontenla, J., McClintock, W.E., Richard, E.C.: 2009, Solar Irradiance Reference Spectra (SIRS) for the 2008 Whole Heliosphere Interval (WHI). *Geophys. Res. Lett.* **36**, L01101. DOI. ADS.
- Woods, T.N., Eparvier, F.G., Harder, J., Snow, M.: 2018, Decoupling solar variability and instrument trends using the Multiple Same-Irradiance-Level (MuSIL) analysis technique. *Solar Phys.* **293**, 76. DOI. ADS.
- Woods, T.N., Harder, J.W., Kopp, G., McCabe, D., Rottman, G., Ryan, S., Snow, M.: 2021, Overview of the Solar Radiation and Climate Experiment (SORCE) seventeen-year mission. *Solar Phys.* **296**, 127. DOI. ADS.
- Woods, T.N., Harder, J.W., Kopp, G., Snow, M.: 2022, Solar cycle variability results from the Solar Radiation and Climate Experiment (SORCE). *Solar Phys.* **297**, 43. DOI.
- Yeo, K.L., Krivova, N.A., Solanki, S.K., Glassmeier, K.H.: 2014, Reconstruction of total and spectral solar irradiance from 1974 to 2013 based on KPVT, SoHO/MDI, and SDO/HMI observations. *Astron. Astrophys.* **570**, A85. DOI. ADS.
- Young, C., Stone, T., Daniels, J., Snow, M., Clark, R., Williams, J.P.: 2021, Extending the spectral range of the RObotic Lunar Observatory (ROLO) model to climate science-relevant wavelengths. In: *AGU Fall Meeting Abs.* agu.confex.com/agu/fm21/meetingapp.cgi/Paper/821655.